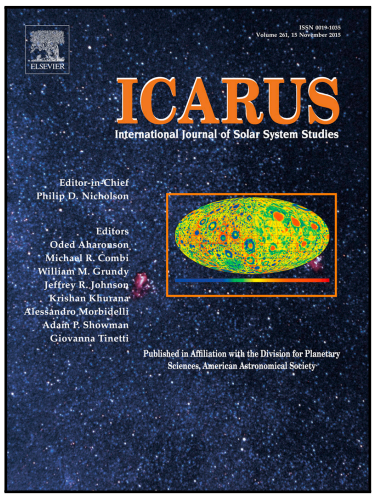

Late-Stage Diagenetic Concretions in the Murray Formation, Gale Crater, Mars

Vivian Z. Sun , Kathryn M. Stack , Linda C. Kah , Lucy Thompson , Woodward Fischer , Amy J. Williams , Sarah S. Johnson , Roger C. Wiens , Rachel E. Kronyak , Marion Nachon , Christopher H. House , Scott VanBommel

PII: S0019-1035(18)30597-9
DOI: https://doi.org/10.1016/j.icarus.2018.12.030
Reference: YICAR 13146

To appear in: *Icarus*

Received date: 17 September 2018
Revised date: 4 December 2018
Accepted date: 12 December 2018

Please cite this article as: Vivian Z. Sun , Kathryn M. Stack , Linda C. Kah , Lucy Thompson , Woodward Fischer , Amy J. Williams , Sarah S. Johnson , Roger C. Wiens , Rachel E. Kronyak , Marion Nachon , Christopher H. House , Scott VanBommel , Late-Stage Diagenetic Concretions in the Murray Formation, Gale Crater, Mars, *Icarus* (2018), doi: https://doi.org/10.1016/j.icarus.2018.12.030

Highlights:

- Concretions exhibit morphologic and chemical diversity throughout the Murray fm.
- Concretions likely formed in multiple fluid episodes with varying chemistry.
- Many concretions likely formed during late diagenesis after sediment compaction.

Late-Stage Diagenetic Concretions in the Murray Formation, Gale Crater, Mars

Vivian Z. Sun*[1], Kathryn M. Stack[1], Linda C. Kah[2], Lucy Thompson[3], Woodward Fischer[4], Amy J. Williams[5], Sarah S. Johnson[6], Roger C. Wiens[7], Rachel E. Kronyak[2], Marion Nachon[8], Christopher H. House[9], Scott VanBommel[10]

[1]Jet Propulsion Laboratory, California Institute of Technology, 4800 Oak Grove Drive, Pasadena, CA 91109
[2]Earth and Planetary Sciences, University of Tennessee, 1621 Cumberland Avenue, Knoxville, TN 37996
[3]Planetary and Space Science Centre, University of New Brunswick, Fredericton, NB E3B 5A3, Canada
[4]Division of Geological and Planetary Sciences, California Institute of Technology, 1200 East California Boulevard, Pasadena, CA 91125
[5]Department of Geological Sciences, University of Florida, Gainesville, FL 32611
[6]Science, Technology, and International Affairs Program, Georgetown University, Washington, DC 20057
[7]Space and Remote Sensing, Los Alamos National Laboratory, Los Alamos, NM 87545
[8]Earth and Planetary Sciences, University of California Davis, 1 Shields Avenue, Davis, CA 95616
[9]Department of Geosciences, Penn State University, University Park, PA 16802
[10]Department of Earth and Planetary Sciences, Washington University in Saint Louis, Saint Louis, MO, 63130, USA

*Corresponding Author:
Vivian Z. Sun
MS 183-301
4800 Oak Grove Drive
Pasadena, CA 91109
(626)314-0121
Vivian.Sun@jpl.caltech.edu

Short Title: Murray formation concretions at Gale crater
Keywords: Mars; concretions; diagenesis; Mars Science Laboratory; Gale crater

Abstract
Concretions are prevalent features in the generally lacustrine deposits of the Murray formation in Gale crater. In this work, we document the morphologic, textural, and chemical properties of these concretions throughout 300 meters of Murray formation stratigraphy from Mars Science Laboratory observations between Sols 750-1900. We interpret these observations to constrain the timing and composition of post-depositional fluid events at Gale crater. We determine that the overall diversity of concretion morphology, size, texture, and chemistry throughout the Murray formation indicates that concretions formed in multiple, likely late diagenetic, episodes with varying fluid chemistries. Four major concretion assemblages are observed at distinct stratigraphic intervals and approximately correlate with major distinct chemical enrichments in Mg-S-Ni-Cl, Mn-P, and Ca-S, among other local enrichments. Different concretion size populations and complex relationships between concretions and veins also suggest multiple precipitation events at Gale crater. Many concretions likely formed during late diagenesis after sediment compaction and lithification, based on observations of concretions preserving primary host rock laminations without differential compaction. An upsection decrease in overall concretion size corresponds to an inferred upsection decrease in porosity and permeability, thus constraining concretion formation as postdating fluid events that produced initial cementation and porosity loss. The combined observations of late diagenetic concretions and distinct chemical enrichments related to concretions allow constraints to be placed on the chemistry of late stage fluids at Gale crater. Collectively, concretion observations from this work and previous studies of other diagenetic features (veins, alteration halos) suggest at least six post-depositional events that occurred at Gale crater after the deposition of the Murray formation.

1. Introduction

The Mars Science Laboratory (MSL) Curiosity rover has been investigating aqueous environments preserved at Gale crater since August 2012. An ongoing focus of the mission is to characterize the timing and duration of past aqueous events, the nature and chemistry of the fluids involved, and to determine the implications for habitability on Mars. Gale crater preserves evidence of both primary fluids, in the form of fluvial and lacustrine deposits (e.g., *Grotzinger et al., 2015; Fedo et al., 2018*), and post-depositional fluid flow, in the form of veins, concretions, and mineral alteration products (**Figure 1**; e.g., *Stack et al., 2014; Siebach et al., 2014; Nachon et al., 2014; 2016; Kah et al., 2015; Kronyak et al., 2015; Caswell and Milliken; 2017; Wiens et al., 2017; Frydenvang et al., 2017; Yen et al., 2017; Kah et al., 2018*). Because the composition of sedimentary materials within Gale crater represents the sum of deposition and post-depositional (i.e. diagenetic) processes, characterizing the origin of diagenetic features is critical to understanding the timing and origin of post-depositional fluid flow events. Thus, diagenetic features may provide a window into fluid chemistry and other environmental conditions present during later stages in Mars' history.

In this work, we focus on concretions – here defined as indurated masses that result from the precipitation of a mineral cement (e.g., *Seilacher, 2001; Mozley, 2003*). These features are typically more resistant to erosion than the surrounding host rock and therefore appear in high relief, or as lag deposits, such as the Meridiani Planum "blueberries" (e.g., *Chan et al., 2004; McLennan et al., 2005*). Concretions form through precipitation of mineral-saturated pore-fluids, and can be triggered by changes in the temperature, fluid pressure, volatile content, or redox state of pore-fluids (e.g., *Allison and Pye, 1994; Gasparatos, 2012*). Concretions can form at any

stage during or after sediment deposition, and concretion growth can continue over an extended period of time spanning syn-depositional to late diagenetic stages (*Selles-Martinez, 1996*).

The physical and chemical properties of concretions reflect the environmental conditions at the time of concretion formation. The size of concretions results from various factors including porosity, permeability, the availability of cementing ions, and time (e.g., *Chan et al., 2005; 2007; Sefton-Nash and Catling, 2008*). The shape of a concretion is controlled by sediment anisotropies with respect to porosity and permeability, and by the direction and magnitude of fluid flow (e.g., *Berner, 1968; McBride et al., 1999; Chan et al., 2005; Marshall and Pirrie, 2013*). Laminations and textures in the concretion and host material, particularly those indicative of "differential compaction," can yield clues as to the timing of concretion formation relative to sediment compaction and lithification (*Raiswell, 1988; Mozley, 1996; Figure 8 in Selles-Martinez, 1996; Lash and Blood, 2004*). Lastly, the chemistry and mineralogy of concretions provides a measure of the compositions of diagenetic fluids and reactions occurring within pore fluids (e.g., *Raiswell and Fisher, 2000; Chan et al., 2004*).

Concretion properties – both chemical and physical (e.g., size, shape, preservation of primary laminations and textures) – can thus yield insight into the host rock conditions at the time of concretion formation as well as the timing and chemistry of diagenetic fluid events. In this study, we conducted a systematic survey of concretions and their properties throughout the 300 meters of Murray formation explored by the Curiosity rover between Sols 750-1900 to address the following questions:

1) What is the timing of concretion formation relative to the petrogenesis of the Murray formation?
2) What were the host rock properties and fluid chemistries involved in the formation of the Murray concretions?
3) How many episodes of aqueous activity do these concretions record? Interpreting these results in the context of previous diagenetic studies, how many aqueous events occurred at Gale crater after the deposition of Murray sediments?

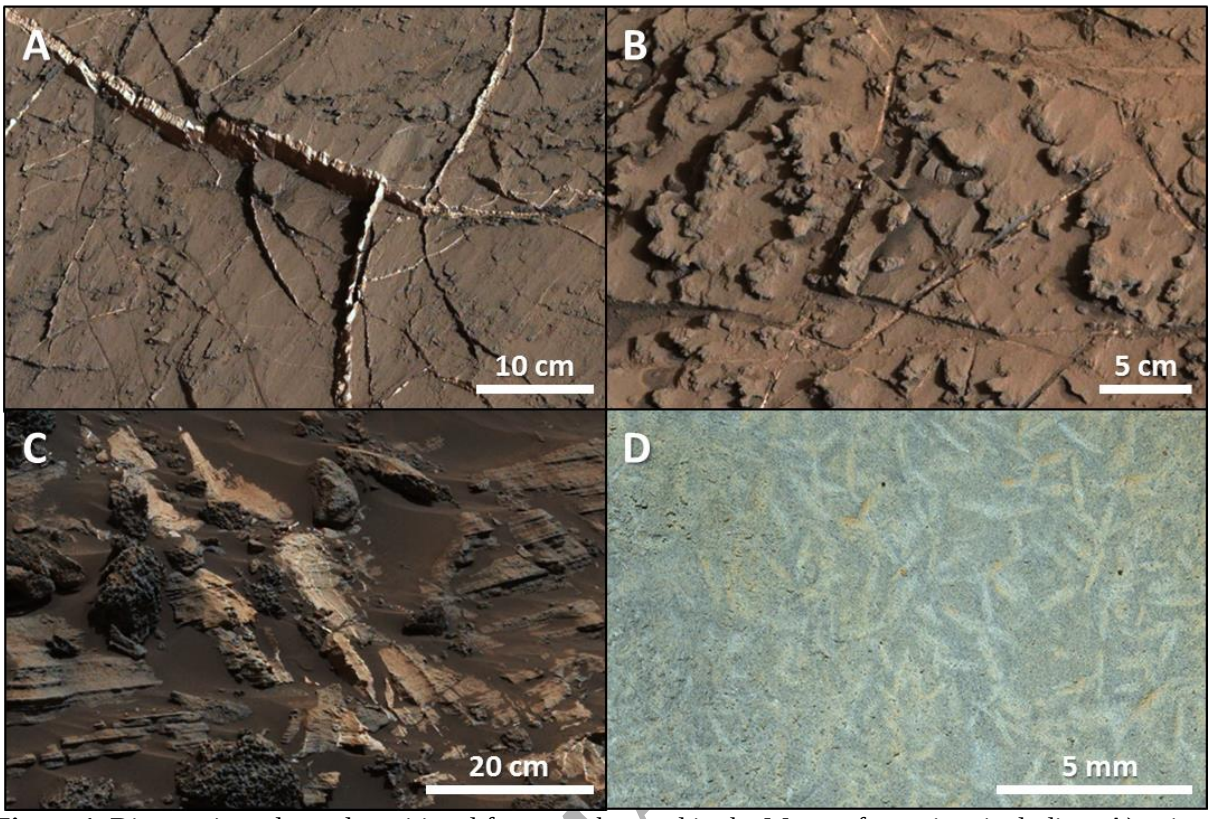

Figure 1. Diagenetic and syn-depositional features observed in the Murray formation, including: A) veins (Sol 1274, mcam05966), B) concretions (Sol 1368, mcam06701), C) alteration halos (Sol 1077, mcam04719), and D) crystal laths (Mojave target on Sol 809, MAHLI 2 cm standoff).

2. Geologic Setting at Gale Crater

The Curiosity rover science team began investigating the sedimentary deposits at Gale crater after landing in August 2012 and spent two years examining the fluvio-lacustrine deposits of the Bradbury group, which is exposed on Gale crater's floor and includes the Yellowknife Bay and Kimberley formations ("YB" and "K" respectively in **Figure 2**; *Grotzinger et al., 2014; Rice et al., 2017*). The team then began exploring the Murray formation, which comprises the basal formation of the Mount Sharp group that forms the central mound in Gale crater. Since September 2014, Curiosity has traversed more than 8.6 kilometers through the Murray formation and documented over 300 meters of Murray stratigraphy.

The Murray formation is composed primarily of finely laminated lacustrine mudstone with intermittent intervals of cross-stratified sandstone, and the thickness of this unit suggests a long-lived (~10^6 years) lacustrine environment in Gale crater (*Grotzinger et al., 2015; Hurowitz et al., 2017; Fedo et al., 2018*). Unconformably overlying the Murray formation is the Stimson formation, an aeolian sandstone that drapes the lacustrine strata of the Murray formation exposed on the present-day slope of Mount Sharp (*Banham et al., 2018*). At the time of writing, the Murray formation has been divided into seven members from stratigraphically oldest to youngest **(Figure 2)**: Pahrump Hills (-4460 to -4435 m), Hartmann's Valley (-4435 to -4415 m), Karasburg (-4415 to -4375 m), Sutton Island (-4375 to -4280 m), Blunts Point (-4280 to -4210 m), Pettegrove Point (-4210 to -4170 m), and Jura (-4170 to -4155 m as of Sol 1900). This section briefly describes these stratigraphic members, which are distinguished on the basis of

grain size, sedimentary structures, color, and other features such as veins, concretions, and desiccation cracks.

The Pahrump Hills member constitutes the most basal exposed member of the Murray formation and preserves a 25-meter-thick sequence reflecting the interfingering of lacustrine mudstone deposits with fluvio-deltaic deposits (*Grotzinger et al., 2014; Stack et al., 2018*). Pahrump Hills is largely composed of finely laminated mudstone at the base that are increasingly interbedded with sandstone layers towards the top of the succession, consistent with its interpretation as a progradational sequence within a lacustrine environment (*Stack et al., 2018*).

The Hartmann's Valley member is stratigraphically above Pahrump Hills and is a 20-meter-thick package of mostly siltstone exhibiting meter-scale trough cross-bedding, consistent with either fluvial or aeolian deposition (*Fedo et al., 2018; Gwizd et al., 2018*). Above Hartmann's Valley lies the 40-meter-thick Karasburg member, which consists of finely-laminated, slightly purple-toned mudstone consistent with lacustrine deposition (*Fedo et al., 2018*). The Karasburg member also hosts the Murray Buttes, a series of buttes where the Murray formation is capped by erosionally resistant sandstone of the Stimson formation.

The Sutton Island member is a 95-meter-thick heterolithic section composed of finely laminated mudstone, centimeter-scale cross-laminated sandstone, and decimeter-scale cross-stratified sandstone consistent with deposition in lake and lake-margin environments (*Fedo et al., 2018*). Additionally, the presence of possible desiccation cracks (*Stein et al., 2018*) suggests intermittent exposure and desiccation of lacustrine deposits.

The 70-meter-thick Blunts Point member is distinguished from the Sutton Island member by abundant Ca-sulfate veins crosscutting finely laminated mudstone. Just above the Blunts Point member are the Pettegrove Point (40-meters-thick) and Jura members (15 meters of which are documented in this work), which together comprise the hematite-bearing topographic feature called Vera Rubin Ridge (*Fraeman et al., 2016*). Preliminary interpretation of sedimentary facies suggests that these members are also composed of finely laminated mudstone, indicative of lacustrine deposition (*Fedo et al., 2018; Edgar et al., 2018*).

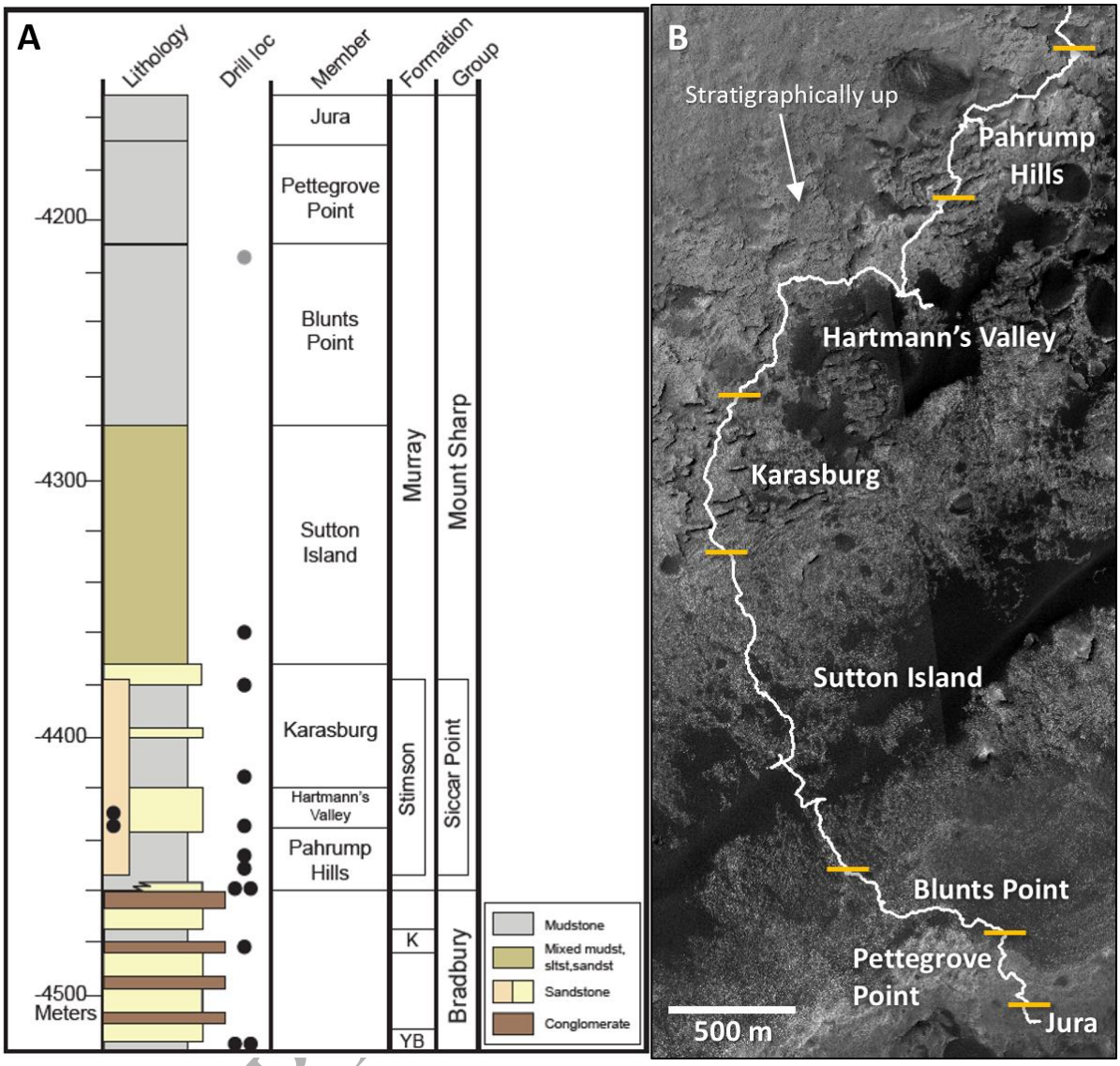

Figure 2. A) A summary stratigraphic column showing the major sedimentary units observed at Gale crater as of Sol 1900, courtesy of the MSL Sedimentology and Stratigraphy group. Black dots correspond to drill sites. **B)** Geographic representation of Curiosity's traverse through the Murray, with approximate boundaries of the seven Murray members marked. In order from stratigraphically oldest to youngest: Pahrump Hills (Sols 750-1100; -4460 to -4435 m), Hartmann's Valley (Sols 1100-1410; -4435 to -4415 m), Karasburg (Sols 1410-1470; -4415 to -4375 m), Sutton Island (Sols 1470-1690; -4375 to -4280 m), Blunts Point (Sols 1690-1800; -4280 to -4210 m), Pettegrove Point (Sols 1800-1870; -4210 to -4170 m), and Jura (Sols 1870-1900+; -4170 to -4155+ m). North is up in all orbital maps. Note that the Blunts Point, Pettegrove Point, and Jura members were further explored by the Curiosity science team after Sol 1900. The sol and elevation ranges described here only apply to observations taken before Sol 1900.

3. Methods

In this work, we conducted a comprehensive survey of concretions in the Murray formation to infer the timing and conditions of their formation. We observed the morphologic and spatial properties of concretions using the Mastcam (Mast Camera) and MAHLI (Mars Hand

Lens Imager) image datasets. Concretion compositions were determined from ChemCam (Chemistry and Camera) and APXS (Alpha Particle X-Ray Spectrometer) data. In this work, we studied all data available from these instruments that were taken between Sols 750-1900. To explore potential changes in concretion morphology or composition through stratigraphy, observations were plotted using elevation as a datum, which is a proxy for stratigraphic position (*Grotzinger et al., 2015*).

We note that there is inherent bias in the datasets produced by a discovery-driven rover mission such as Curiosity. Observations and measurements tend to be focused on bedrock targets and diagenetic features that draw our attention, when in reality there may exist lateral heterogeneities at a single stratigraphic level. However, it is difficult to correct for these heterogeneities in data analysis when the real extent of these heterogeneities cannot be feasibly explored in a mission's lifetime. Here we acknowledge these uncertainties and avoid imparting further observational bias in our analyses by reporting results from all image and compositional datasets available at concretion-relevant resolutions during Curiosity's traverse.

3.1 Image Datasets (Mastcam, MAHLI)

Mastcam images provide a large dataset with both broad-scale context and resolution sufficient to resolve centimeter-scale features like concretions (*Bell et al., 2017*). Mastcam images taken from Sols 750 to 1900 were examined to determine the absence or presence of concretions, and to characterize concretion morphology and texture **(Section 4)**. The results presented here represent near-field Mastcam images with resolutions sufficient to resolve concretion morphologies; these resolutions were typically 0.14 to ~1 mm/pixel at standoff distances of 1.8 to 6 meters. Possible concretions were occasionally observed in mid- to far-field images, but lower resolution did not permit discrimination of specific concretion morphologies. In total, we analyzed 1732 Mastcam observations **(Supporting Table 1)**, which encompassed single image frames and mosaics from both the left and right cameras. Of these, 1200 observations were identified as containing concretions.

Images from the MAHLI camera were also used in this study to examine concretions in detail. MAHLI images are typically obtained of select targets observed in the overlapping Mastcam images, and the higher MAHLI resolutions are especially useful for identifying smaller concretions that are not visible at Mastcam resolutions. We examined MAHLI images of 299 bedrock targets **(Supporting Table 2)**. Each target is often imaged multiple times at different standoff distances, commonly at 25, 5, and either 2 or 1 cm, corresponding to image resolutions ranging from 16 to 100 microns/pixel (*Edgett et al., 201*2). Of these bedrock targets, we found 172 targets that contained concretions in a MAHLI image.

Concretion sizes were estimated for a subset of Mastcam images to illustrate qualitative trends in concretion size with elevation. Due to the large size of the Mastcam dataset, a subset of Mastcam images was selected to document concretion size trends throughout the traverse. After every drive, Curiosity typically takes a Mastcam workspace mosaic at the end-of-drive location. We identified 124 rover locations spanning Sols 750-1900 where concretions were visible in the Mastcam workspace mosaics, and measured the sizes of the largest concretions present. In each workspace, the apparent largest concretions were first selected by visual inspection, and then measured by multiplying the number of pixels spanned by the concretion diameter with the distance from the mast and the instantaneous field of view (IFOV) for the left or right Mast cameras. The size of the largest concretion was noted for each workspace mosaic. In 11 workspaces where only small-scale concretions were present below Mastcam resolution, we

approximated the maximum concretion size in those workspaces from MAHLI images. We note that these measurements are only meant to qualitatively illustrate overall size trends throughout the 300 meter Murray section; a more detailed and statistically robust assessment of concretion size populations was made in a separate task using only MAHLI images (see below).

Concretion size populations were then determined at greater detail by measuring all concretions observed in 50 MAHLI targets. Concretion sizes were determined by measuring the number of pixels spanned by the concretion diameter relative to the image resolution for the given standoff distance. Because MAHLI images are not obtained systematically (compared to Mastcam images) and do not uniformly span the 300 meters of Murray section studied in this work, we binned these results by Murray member to generate histogram results for each member.

Relative concretion density was also estimated for each of the 1200 Mastcam observations containing concretions and was categorized as having "low," "medium," or "high" concretion density **(Figure 3)**. Generally, a "low density" is designated when concretions occupy approximately less than ~1% of the visible rock surface, a "medium density" is designated when concretions occupy between 1-30% of the visible rock surface, and a "high density" is designated when concretions occupy more than ~30% of the visible rock surface. Similar to the Mastcam concretion size approximations, these Mastcam concretion density assessments are meant to qualitatively illustrate overall density trends throughout the 300 meter Murray section.

Nearest neighbor statistics (e.g., *Clark and Evans, 1954*) were also calculated for concretions identified on flat-lying bedrock in 44 MAHLI targets using ArcGIS software. Concretions were marked in a separate shapefile for each MAHLI image and the bedrock surface area was determined. The Average Nearest Neighbor tool in the ArcGIS Spatial Statistics Toolbox was used to calculate the average absolute distance from each concretion to its nearest neighboring concretion. Absolute measurements of distance and concretion size are possible from MAHLI images because the images considered here are taken approximately perpendicular to the flat-lying bedrock surface and dimensions can be calculated based on the known image resolution at a given standoff distance. This average distance was then ratioed to the expected average distance for features that are randomly distributed on the prescribed surface area. A resulting ratio of less than one suggests clustering, whereas a ratio greater than one suggests dispersion.

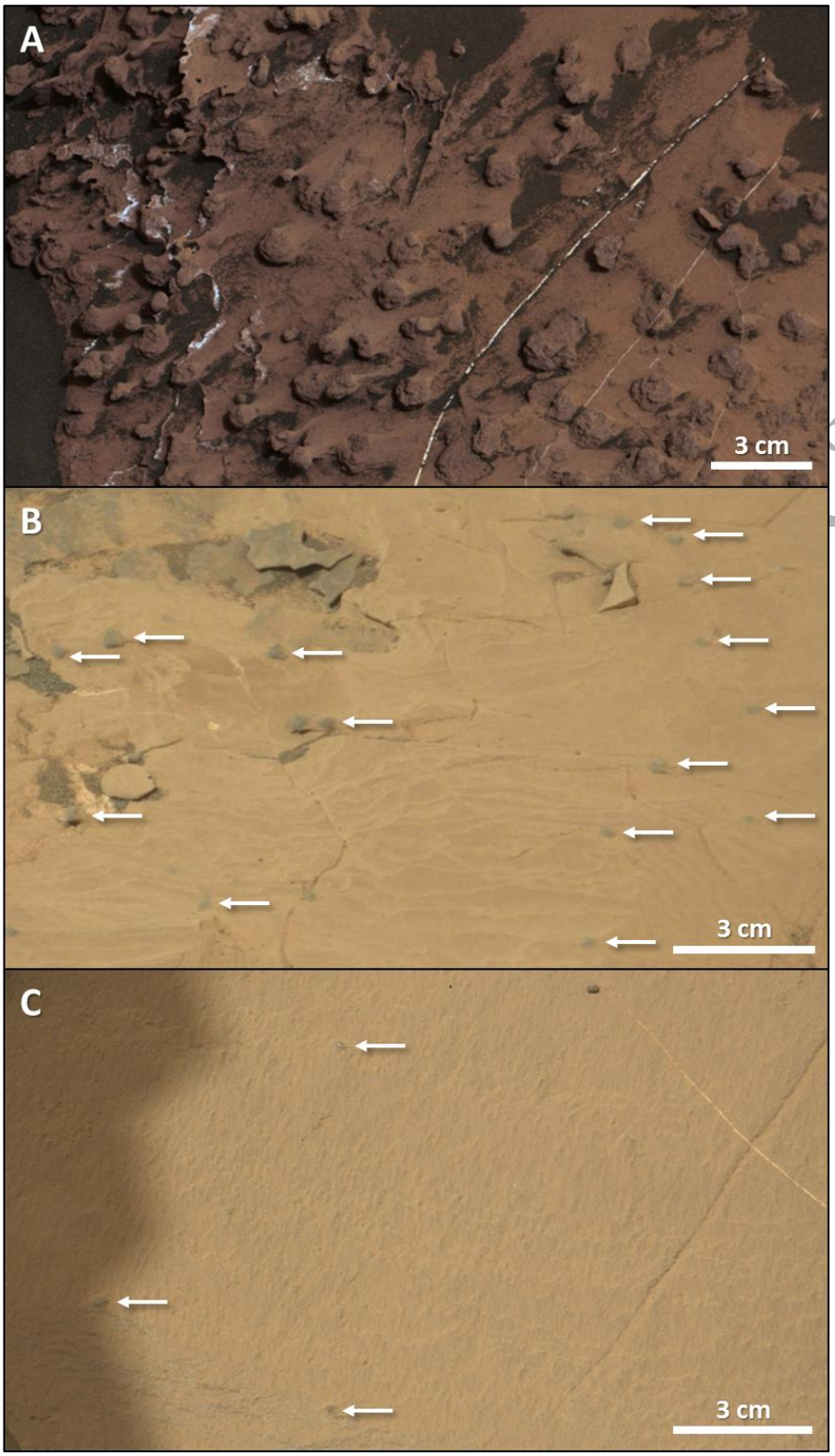

Figure 3. Examples of **A)** High (Chitembo on Sol 1480, mcam07429), **B)** Medium (Old_Point on Sol 1724, mcam08996), and **C)** Low concretion density (Sol 1423, mcam07022). Arrows in B) and C) indicate the concretions in the scene.

3.2 Geochemical Datasets (ChemCam, APXS)

Elemental compositions of concretions and concretion-rich targets were obtained from the ChemCam and APXS instruments. The ChemCam instrument acquires point-by-point compositional information of remote targets using laser-induced breakdown spectroscopy (LIBS; *Wiens et al., 2012; Maurice et al., 2012*). In this work, we use the major element (Si, Ti, Al, Fe, Mg, Ca, Na, K; *Clegg et al., 2017*) compositions of 74 ChemCam targets that hit a concretion in at least one LIBS point in a raster or line scan observation. We report the ChemCam results as the elemental enrichment of the concretion relative to the host rock, to avoid complications arising from variation in the overall composition of the host rock (cf. *Thompson et al., 2017*). For each ChemCam observation, we determined an average concretion composition from LIBS spectra of concretion targets and an average host rock composition from LIBS spectra of Murray bedrock at each location.

APXS compositional data was also obtained for 115 targets that were determined to contain concretions in the APXS field of view (FOV). The APXS instrument acquires chemical compositions (Na, Mg, Al, Si, P, S, Cl, K, Ca, Ti, Cr, Mn, Fe, Ni, Zn, Br) of samples using a combination of particle-induced X-ray emission and X-ray fluorescence (*Gellert and Clark, 2015*). The compositions reported here represent a combination of concretion and host rock compositions visible in the APXS FOV. It is not possible to derive unique solutions for concretion compositions from single APXS measurements (*VanBommel et al., 2016*). We therefore compare the compositions of concretion-bearing bedrock to concretion-free bedrock in the same region of stratigraphy. While not a direct measurement of concretion composition, this method enables an approximation of the elemental enrichments present in concretion-rich targets relative to nearby, concretion-free bedrock.

4. Concretions of the Murray Formation

4.1 Concretion Morphologies

Four main morphologic groups of concretions were observed in the Murray formation: dendrites, spherules, irregular, and flat concretions. In this section, we show examples of these concretion types and describe the range of variations that can be observed in color, shape, size, and preservation of primary lamination within these morphologic groups. We additionally describe what we term "lamination-enhancing features," which are erosionally-resistant features that may be related to concretions.

4.1.1 Spherules

"Spherules" are concretions with spherical to sub-spherical shapes **(Figure 4)**, and occur throughout the Murray formation (except in the Jura member), but are most prevalent in the Karasburg, Sutton Island, and Blunts Point members. The colors of spherules can vary from brown-grey tones to dark grey but tend to be darker than the surrounding host rock. Their textures are often smoother than that of the host rock, with dimpled textures sometimes observed in high-resolution MAHLI images **(Figure 4C-E)**. Several spherule occurrences have latitudinal ridges or indentations spanning their periphery (cf. *Chan et al., 2004*), although these examples have only been observed in spherules that have been fully eroded from host rock material **(Figure 4D,E)**. Instances of conjoined spherules, forming doublet and triplet shapes, are also observed but are relatively rare **(Figure 4F,G)**. In situ spherules have sizes that range from 0.3 to 5.6 mm in diameter. Smaller spherules may also occur, but these are below the resolution of the

primary Mastcam image dataset. A single, anomalously large spherule, which has a minimum diameter of 30 mm, has also been observed in the target Viana in the Karasburg member **(Figure 14C)**.

Cross-sections of spherules are very rarely observed in the Murray formation, hence it is difficult to determine if these spherules contain internal structures such as concentric rings or rinds (cf., *Chan et al., 2004*). We identified less than a dozen putative hollow spherules throughout more than 300 m of Murray stratigraphy **(Figure 5)**. These putative hollow spherules tend to occur as loose float materials **(Figure 5A,B,D-F)**, although a small number of examples are observed in situ **(Figure 5C,G)**. These features can be completely hollow and appear as a shell-like feature **(Figure 5B,D-F)**, or they may appear as a rind around a central "core" **(Figure 5A)** or interior material that is similar to the host rock **(Figure 5C,G)**.

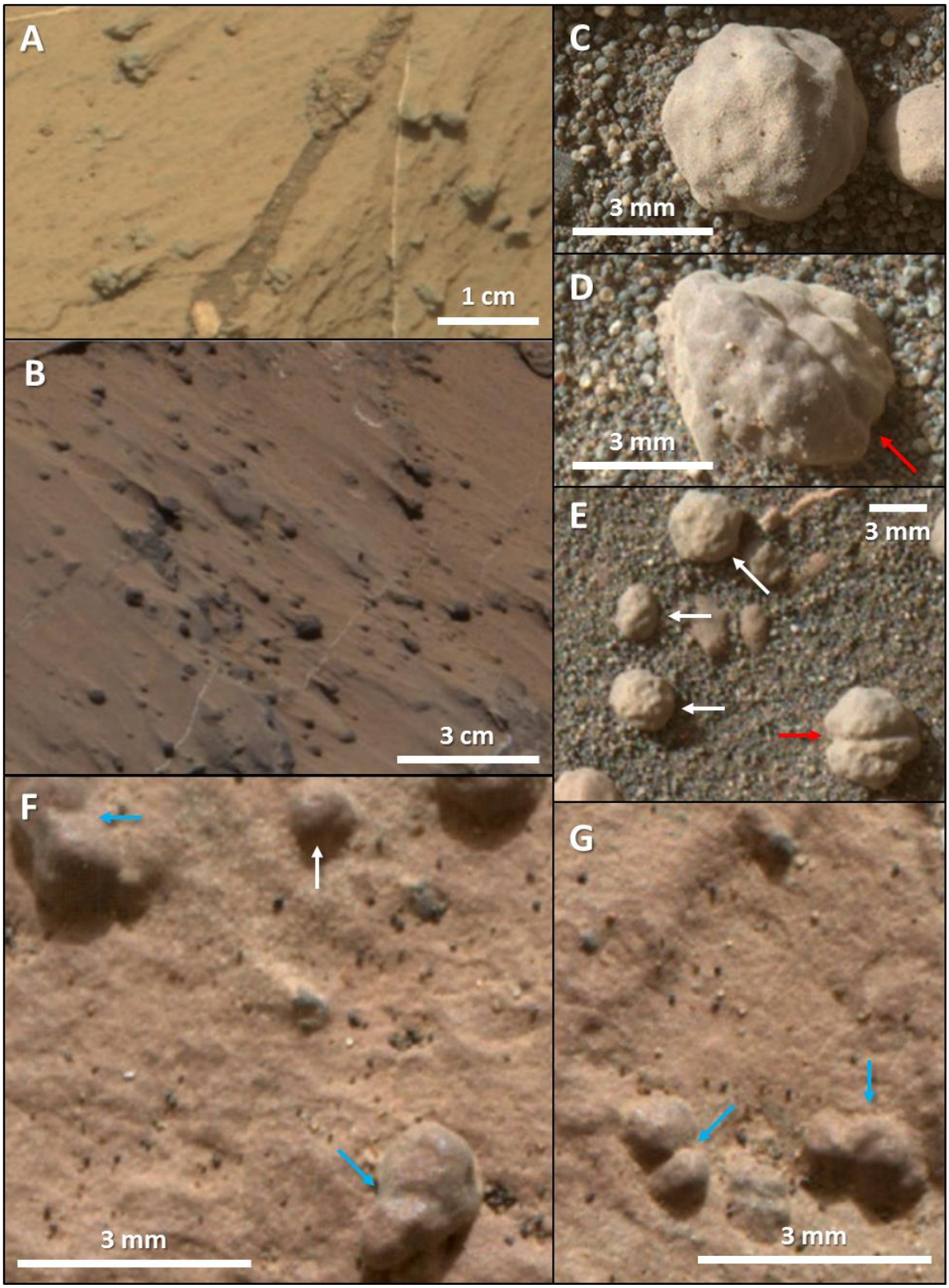

Figure 4. Examples of spherules. **A)** Small spherules in the Mission target in Pahrump Hills (Sol 997, mcam04408). **B)** Prevalent small spherules in the Karasburg member (Sol 1439, mcam07142). **C-E)**

Arrows point to likely spherules occurring as loose float materials in the Gunning_Rocks target in Pettegrove Point (Sol 1806, MAHLI 6 and 25 cm standoff). Red arrows point to spherules with latitudinal ridge-like features. **F-G)** Blue arrows point to conjoined doublet and triplet spherules in the Whiskey target in Sutton Island (Sol 1600, MAHLI 5 cm standoff).

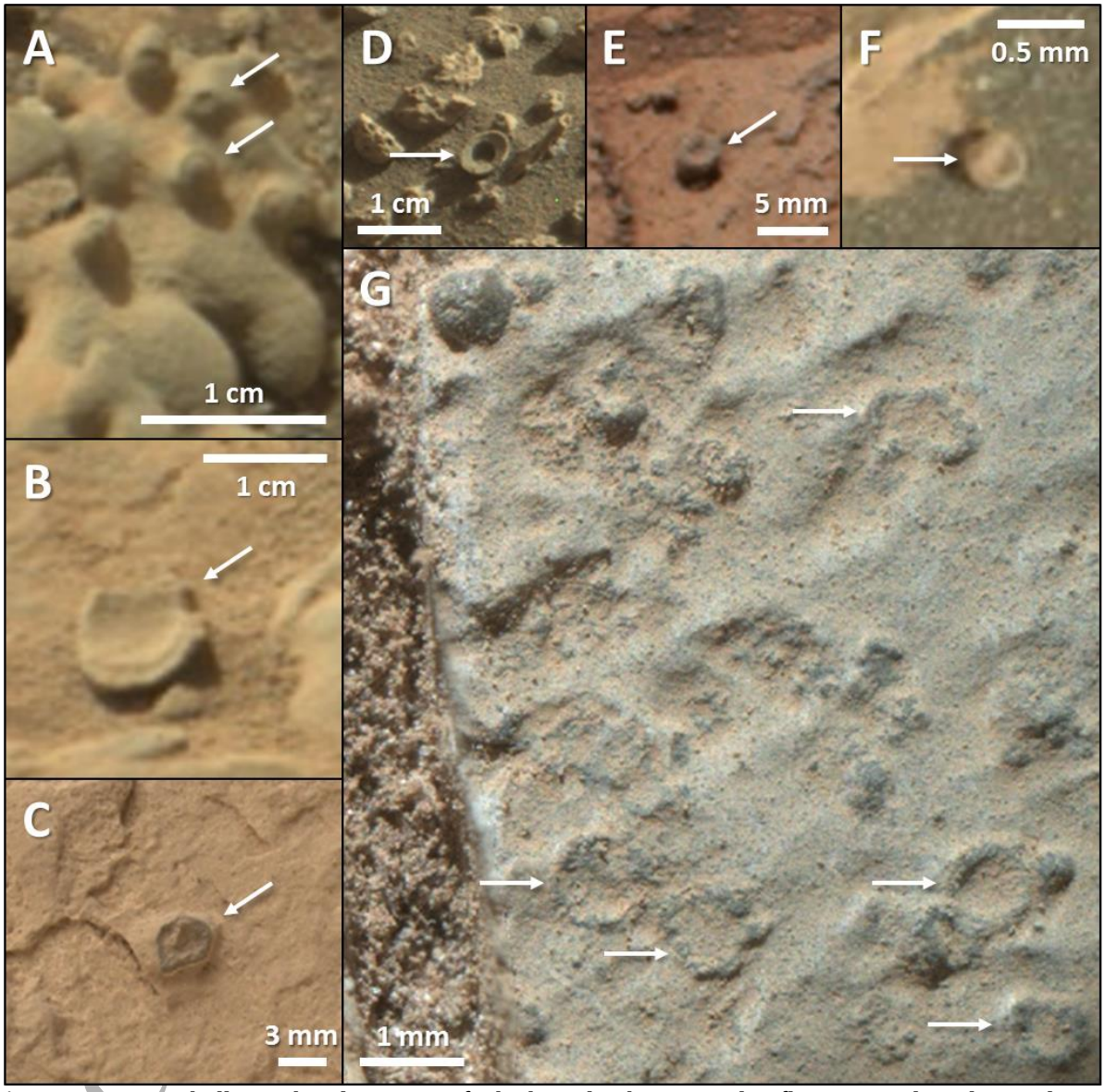

Figure 5. Putative hollow spherules, many of which tend to be exposed in float materials and are only rarely observed in situ. **A)** Hollow, dimple-like features in a float rock possibly formed from an aggregation of multiple concretions (Sol 995, mcam04405). **B)** A hollow shell-like float rock (Sol 1280, mcam06019). **C)** An in situ example of a possible hollow concretion in the Fern_Spring target (Sol 1702, MAHLI 25 cm standoff). **D)** A ring-like feature (Sol 1185, mcam05376). **E)** A dimple-like feature in an in situ spherule (Sol 780, mcam03401). **F)** A hollow shell-like feature (Sol 1797, mcam09279). **G)** Several instances of hollow spherules embedded in the Schwarzand rock target (Sol 1273, MAHLI 5 cm standoff).

4.1.2 Flat

"Flat" concretions are characterized by irregular two-dimensional shapes and a limited thickness in the vertical dimension **(Figure 6)**. Occasionally, these concretions may exhibit ellipsoidal shapes **(Figure 6B)**. Flat concretions are only observed in the Karasburg to Pettegrove Point members and exhibit color variations from red to grey or black, with some color variation occurring in closely-spaced concretions **(Figure 6C)**. These features appear smoother-textured than the host rock and often occur along bedding planes, occasionally coalescing to form contiguous sheets **(Figure 6A,D)**. Flat concretions range from the sub-millimeter scale for individual concretions to the decimeter scale when forming contiguous sheets. Variations in texture and associated chemical enrichments within this flat concretion category were further investigated in *Meslin et al.* (2018).

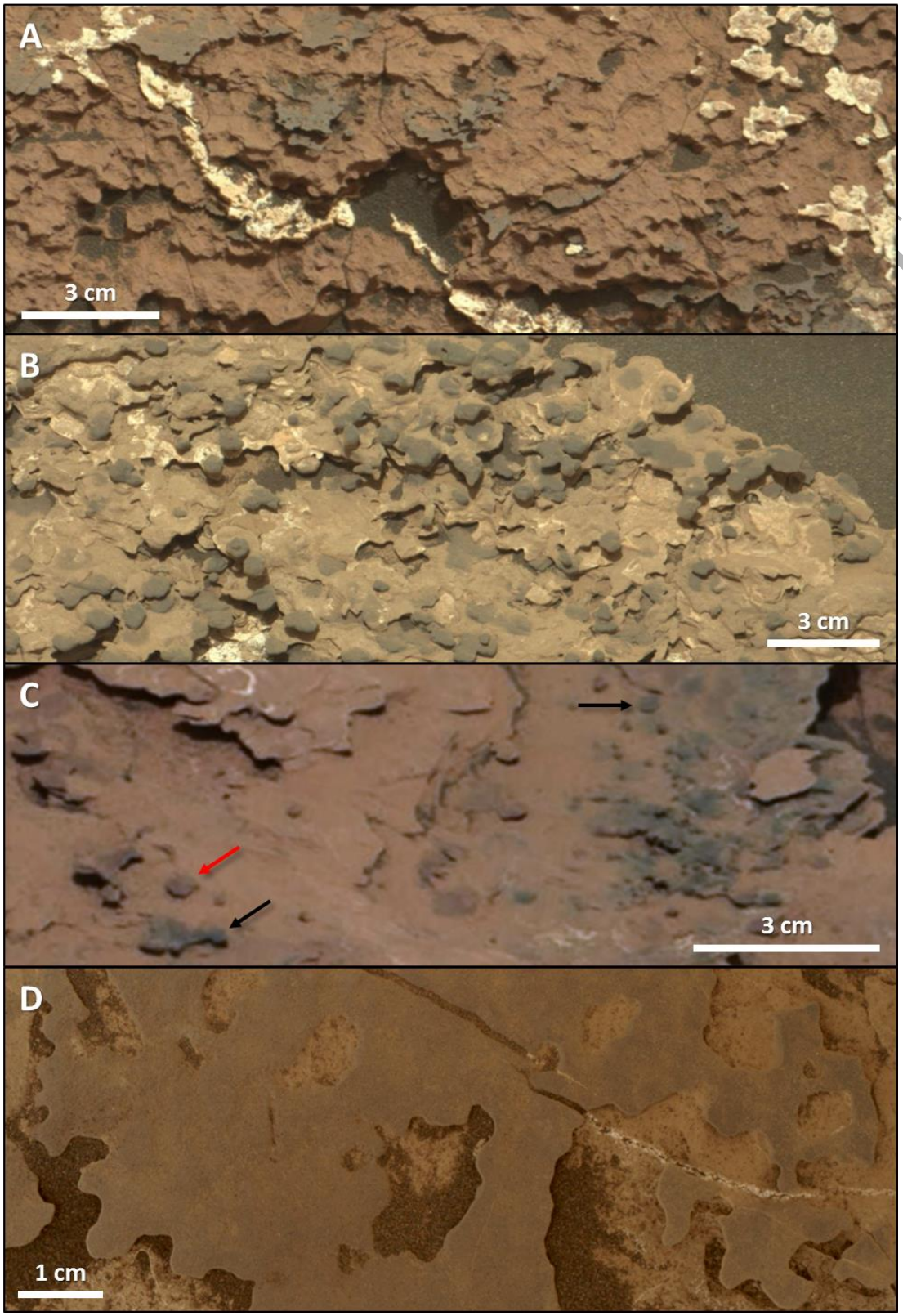

Figure 6. Examples of flat concretions. **A)** Swaths of grey-toned concretions that form contiguous sheets in the Blueberry_Mountain target in Sutton Island (Sol 1661, mcam08625). **B)** Some flat grey concretions

exhibit almost lensoidal shapes and transition to contiguous sheet-like expressions, as shown in the Fernald_Point target in Blunts Point (Sol 1728, mcam09025). **C)** Color variations from red (red arrows) to grey or black (black arrows) are observed in flat concretions in the Damariscotta target in Blunts Point (Sol 1753, mcam09164). **D)** Sheets of flat concretions often conform to the underlying bedrock, as seen in the Jones_Marsh target in Blunts Point (Sol 1727, MAHLI 5 cm standoff).

4.1.3 Irregular

The "irregular" group of concretions encompasses discrete concretions (i.e. those with defined boundaries that differentiate them from host rock materials) that are not spheroidal, flat, or dendritic **(Figure 7)**. These features are found in all Murray formation members, but exhibit variations in shape between different members. Irregular concretions in the Pahrump Hills to Sutton Island members can exhibit larger lateral dimensions than vertical dimensions **(Figure 7A-C,E)**, whereas those in the Pettegrove Point member notably take on a "teardrop" shape **(Figure 7G)**. Anomalously large and dark protrusions are observed at one location in the Jura member (at -4158 m elevation), which have not been observed elsewhere during the Murray traverse **(Figure 7F)**. Irregular concretions exhibit both coloration similar to the host rock and coloration darker than the host rock; colors can vary from grey to brown to red. Texturally, this group can be subdivided into smooth-textured irregular concretions **(Figure 7C,D,F,G)** and rough-textured irregular concretions **(Figure 7A,B,E)**. Irregular concretions span a wide range of sizes; the smallest are on the order of 1 mm and the largest can reach sizes greater than 30 mm in the longest dimension.

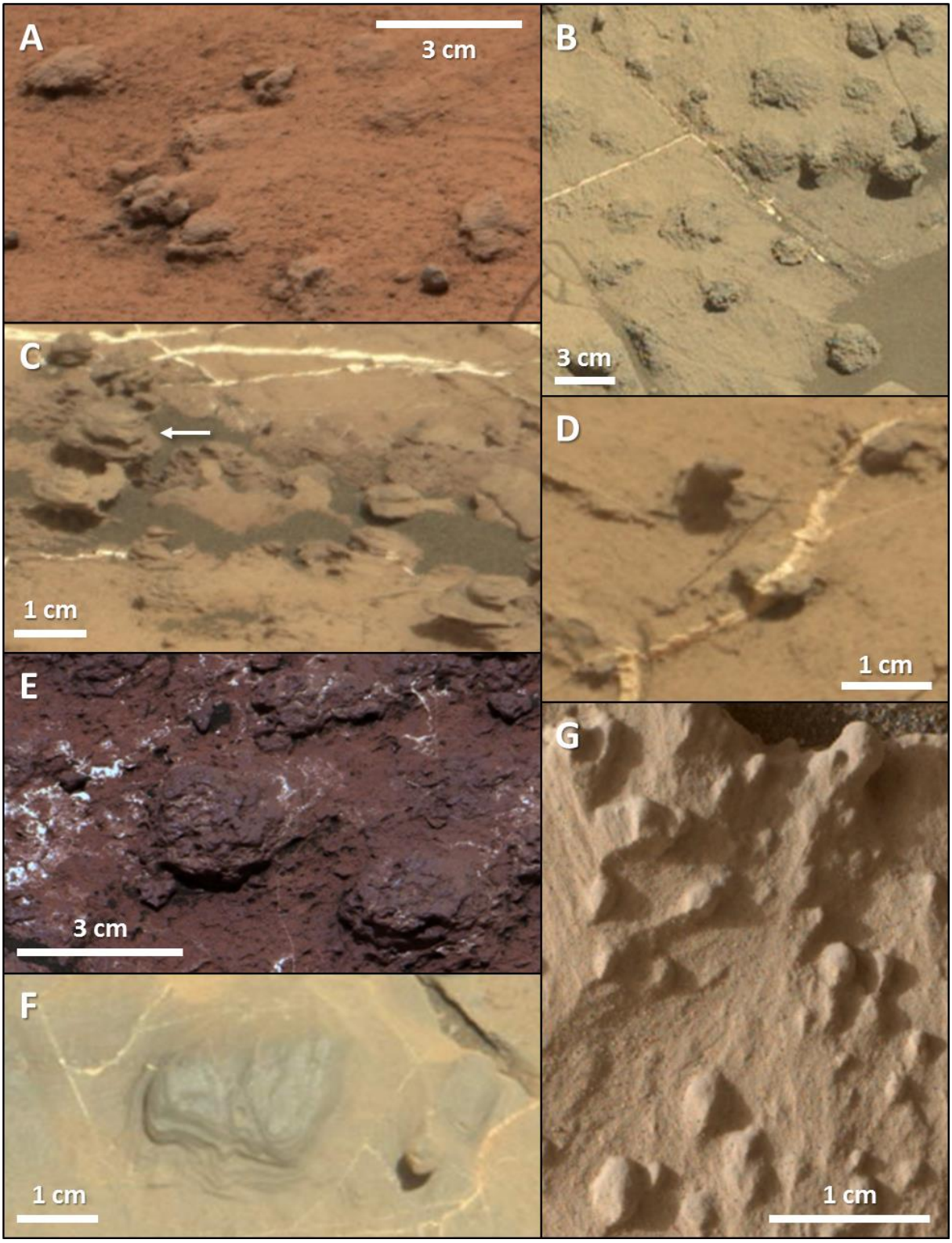

Figure 7. Examples of irregular concretions. **A)** Rough textured grey irregular concretions in the Shoemaker target in Pahrump Hills (Sol 799, mcam03494). **B)** Rough-textured concretions in the Hartmann's Valley member (Sol 1171, mcam05310). **C)** Arrow points to a smooth-textured irregular

concretion that appears to preserve the original host rock laminations within the concretion body, observed in the Nokaneng target in Karasburg (Sol 1497, mcam07579). **D)** Smooth-textured irregular concretions in the Donkerbos target in Karasburg (Sol 1454, mcam07190). **E)** Rough and lumpy-textured irregular concretions in the Sawmill target in Sutton Island (Sol 1578, mcam08038). **F)** Anomalously large, dark, and irregular protrusions are observed in the Pongola target in the Jura member (Sol 1891, mcam09907). **G)** Teardrop-shaped irregular concretions are observed in the Troll_Valley target in Pettegrove Point (Sol 1824, MAHLI 25 cm standoff).

4.1.4 Dendrites

"Dendrites" are concretionary structures consisting of clusters of elongate laths that extend outward from a central point or line **(Figure 8)**. Dendrites are observed in the Murray only at the base of the Pahrump Hills member, at an elevation of approximately -4460 m. These features generally exhibit similar coloration as the surrounding host rock, but can be distinguished from the host rock by their distinctive shapes in relief and smoother surface textures. These features have variable sizes but can reach diameters of up to 3.0-5.5 cm, with individual branches ranging between 0.2-0.4 cm in width and 0.6-3.0 cm in length (*Kah et al., 2015; Nachon et al., 2016; Minitti et al., 2018*). Dendrites are typically observed along bedding planes in the Murray host rock **(Figure 8B,C)** or along fractures and light-toned veins **(Figure 8A,D)**, but some examples can crosscut bedding planes, with no deformation of the host rock (*Minitti et al., 2018*).

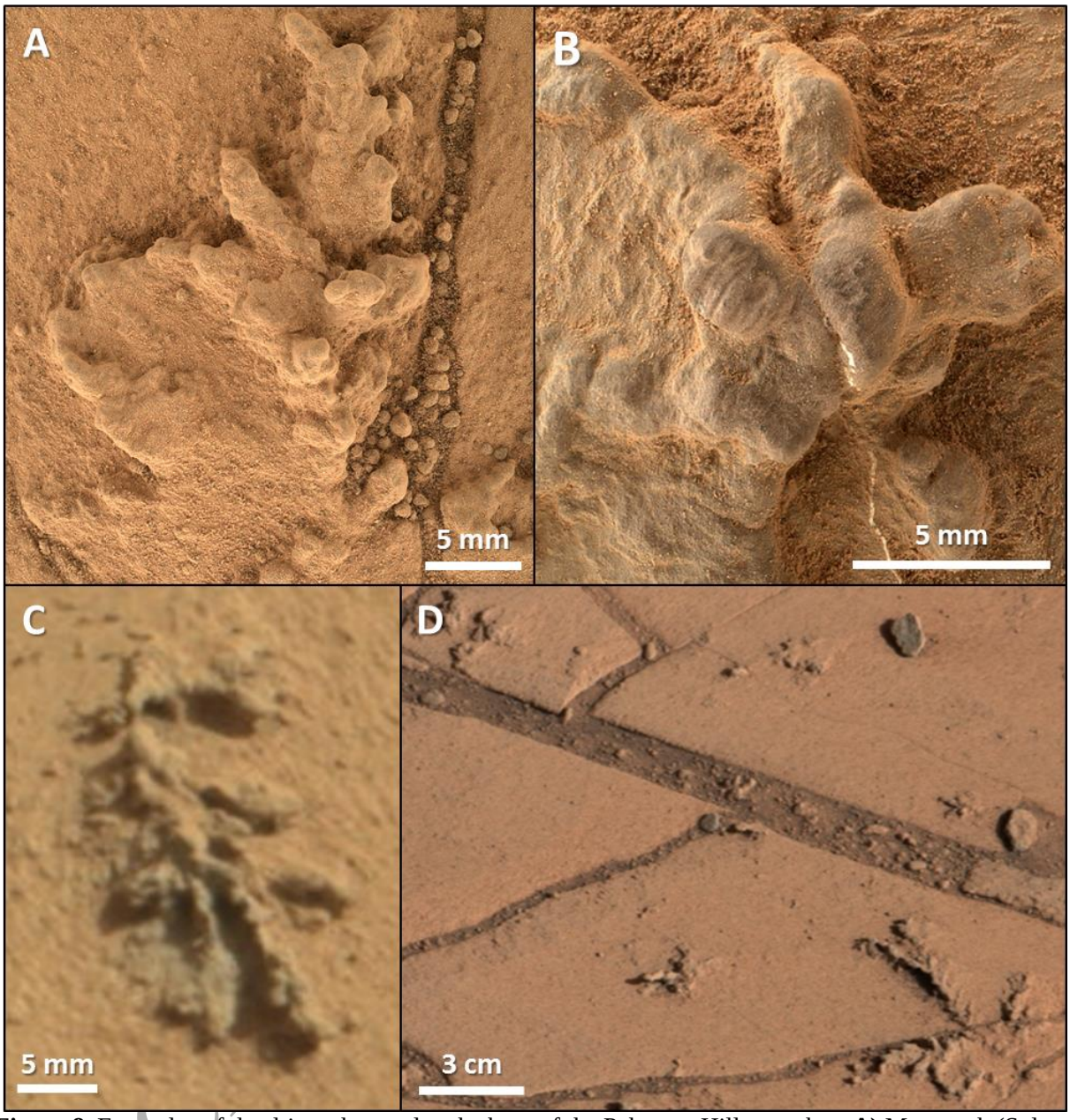

Figure 8. Examples of dendrites observed at the base of the Pahrump Hills member: **A)** Mammoth (Sol 758, MAHLI 5 cm standoff), **B)** Moenkopi, observed to stem from a central sulfate vein (Sol 767, MAHLI 2 cm standoff), **C)** Quartz_Spring (Sol 767, mcam03304), **D)** part of the Sol 753 mcam03237 mosaic.

4.1.5 Lamination-Enhancing Features

Finally, we observe features that we term "lamination-enhancing features," which are erosionally-resistant features that tend to occur along and enhance host rock bedding planes. Unlike discrete concretions, lamination-enhancing features are indistinguishable from the host rock in terms of color and surface microtexture **(Figure 9)**. These features occur in all Murray formation members and can manifest as larger centimeter-scale **(Figure 9A)** or as smaller millimeter-scale bumpy textures **(Figure 9B)**.

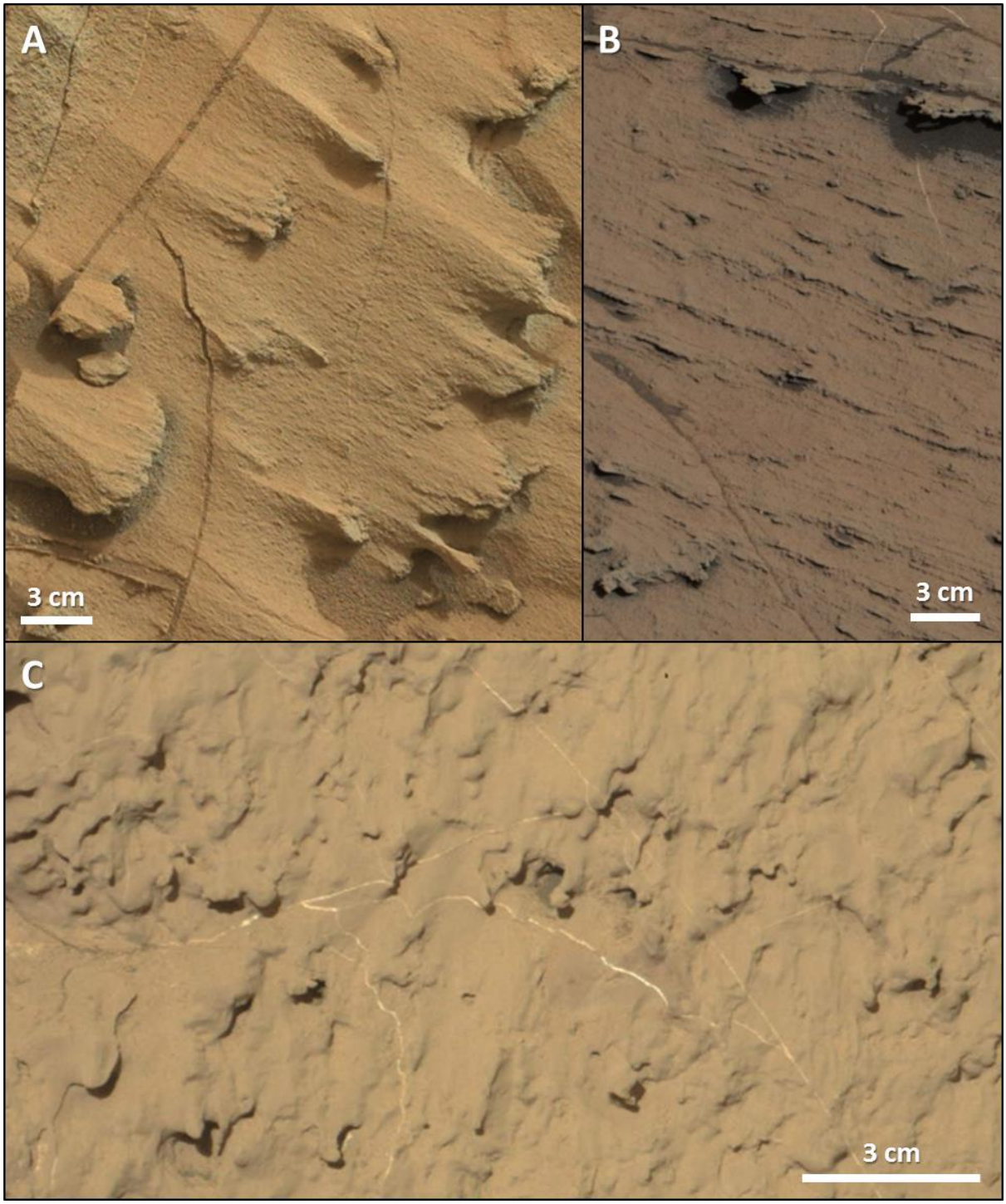

Figure 9. Examples of lamination-enhancing features in: **A)** Pahrump Hills (Sol 785, mcam03423), **B)** Hartmann's Valley (Sol 1104, mcam04893), and **C)** the Cheshire target in Pettegrove Point (Sol 1837, mcam09634).

4.2 Stratigraphic Distribution

Concretions are observed throughout almost the entire 300 m thick Murray formation traversed from Sols 750-1900 **(Figure 10A)**, but certain concretion morphologies are dominant in different Murray members **(Figure 10B,C, 11)**, resulting in four distinct concretion assemblages that are observed.

The first assemblage, occurring in the basal Pahrump Hills member, at -4460 m elevation, hosts an assemblage of dendrites, irregular concretions, and occasional spherules. This region is notable in that it is the only interval in the Murray formation observed to be dominated by dendrites **(Figure 8)**. The second assemblage occurs in the upper Pahrump Hills member and extends through the Hartmann's Valley member (-4460 to -4415 m elevation). This assemblage is dominated by rough-textured, irregular concretions with occasional spherules **(Figure 4A, Figure 7A,B)**.

The Karasburg member marks a transition in terms of concretion assemblages. In contrast to the Pahrump Hills and Hartmann's Valley members, the Karasburg, Sutton Island, and Blunts Point members (-4415 m to -4210 m elevation) contain abundant spherules **(Figure 4B,F,G)**, smooth-textured irregular concretions **(Figure 7C-E)**, and flat concretions **(Figure 6)**. Notably, flat concretions were not observed in the underlying Pahrump Hills and Hartmann's Valley members. Despite an overall similarity in concretion morphologies, the Karasburg, Sutton Island, and Blunts Point members record varying proportions of spherules, irregular, and flat concretions.

The assemblage of concretions changes again in the overlying Pettegrove Point and Jura members (-4210 m to -4155 m elevation). In the lower half of the Pettegrove Point member, flat concretions are no longer observed, and the concretion morphologies are dominated by millimeter-scale, smooth-textured, "teardrop"-shaped irregular concretions **(Figure 7G)** with occasional spherules. The portion of the Jura member explored through Sol 1900 noticeably lacks concretions, except for anomalously large and dark protrusions observed at one locality **(Figure 7F)**. Lamination-enhancing features are present throughout the entire Murray formation **(Figure 9)**, but are only indicated in **Figure 10** if discrete concretion morphologies (dendrites, spherules, flat, irregular concretions) were not observed.

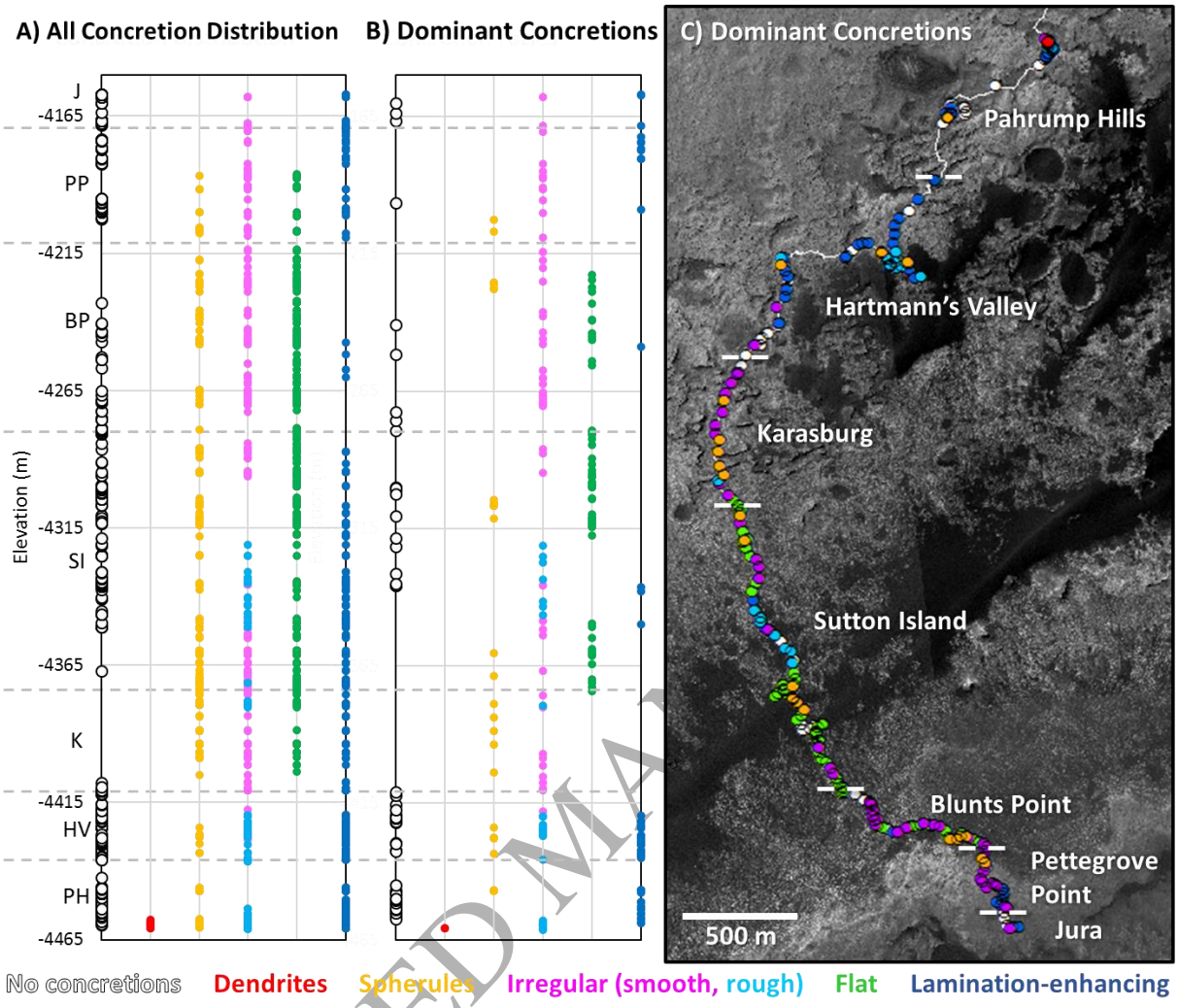

Figure 10. A) Stratigraphic distribution of all concretion morphologies observed throughout the Murray formation from Sols 750-1900. Each point represents a Mastcam or MAHLI observation and the elevation of that observation. Colored points correspond to dendrites, spherules, irregular, and flat concretions as well as lamination-enhancing features. White points indicate where concretions were not observed in the Mastcam or MAHLI scene. **B)** Condensed version of A), showing the stratigraphic distribution of the dominant concretion type observed at each rover location. Each point represents an end-of-drive location and the elevation of that location. **C)** Geographic distribution of B), showing the dominant concretion type along Curiosity's traverse. Each point represents an end-of-drive location and the color corresponds to the dominant concretion morphology or concretion facies observed. PH = Pahrump Hills, HV = Hartmann's Valley, K = Karasburg, SI = Sutton Island, BP = Blunts Point, PP = Pettegrove Point, J = Jura.

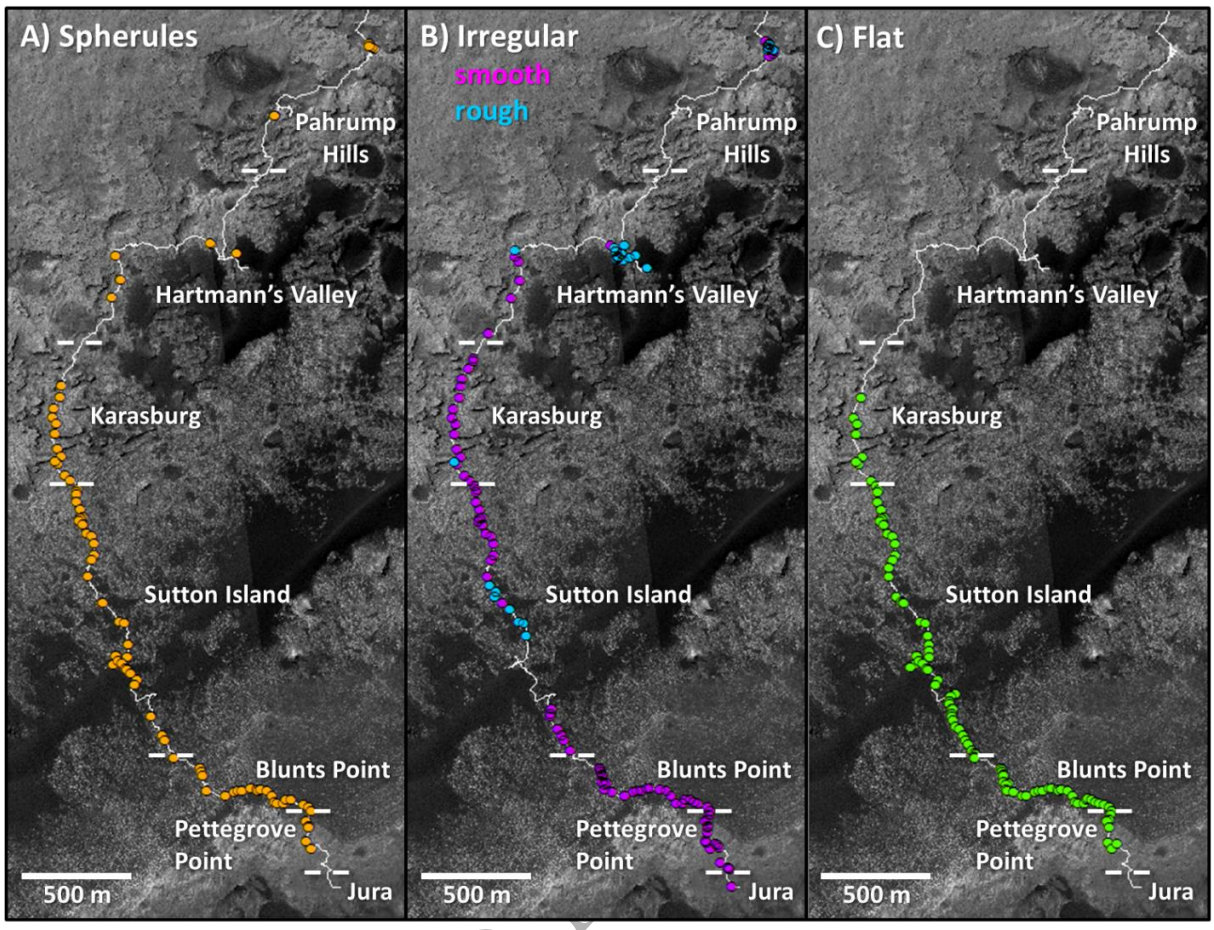

Figure 11. Distribution of **A)** spherules, **B)** irregular concretions, subdivided into smooth-textured and rough-textured, and **C)** flat concretions along Curiosity's traverse through the Murray formation. Each colored point represents an end-of-drive location where the corresponding concretion morphology was observed in Mastcam or MAHLI images obtained from that location.

4.3 Preservation of Primary Laminations

A number of concretions in the Murray formation are observed with laminations along their periphery that appear to be the preserved remnants of the primary host rock laminations **(Figure 4C-E, 7C, 12)**. These preserved laminations seem to occur without any warping at the boundary between the concretion and host rock, and no concretions are observed to deflect host rock laminations. Overall, examples of concretions preserving primary laminations are observed in all of the Murray members **(Figure 13)**. However, there are also many instances where the concretion and host rock laminations are not obvious **(Figure 3A, 7E)** or where laminations are too small or below image resolution to resolve.

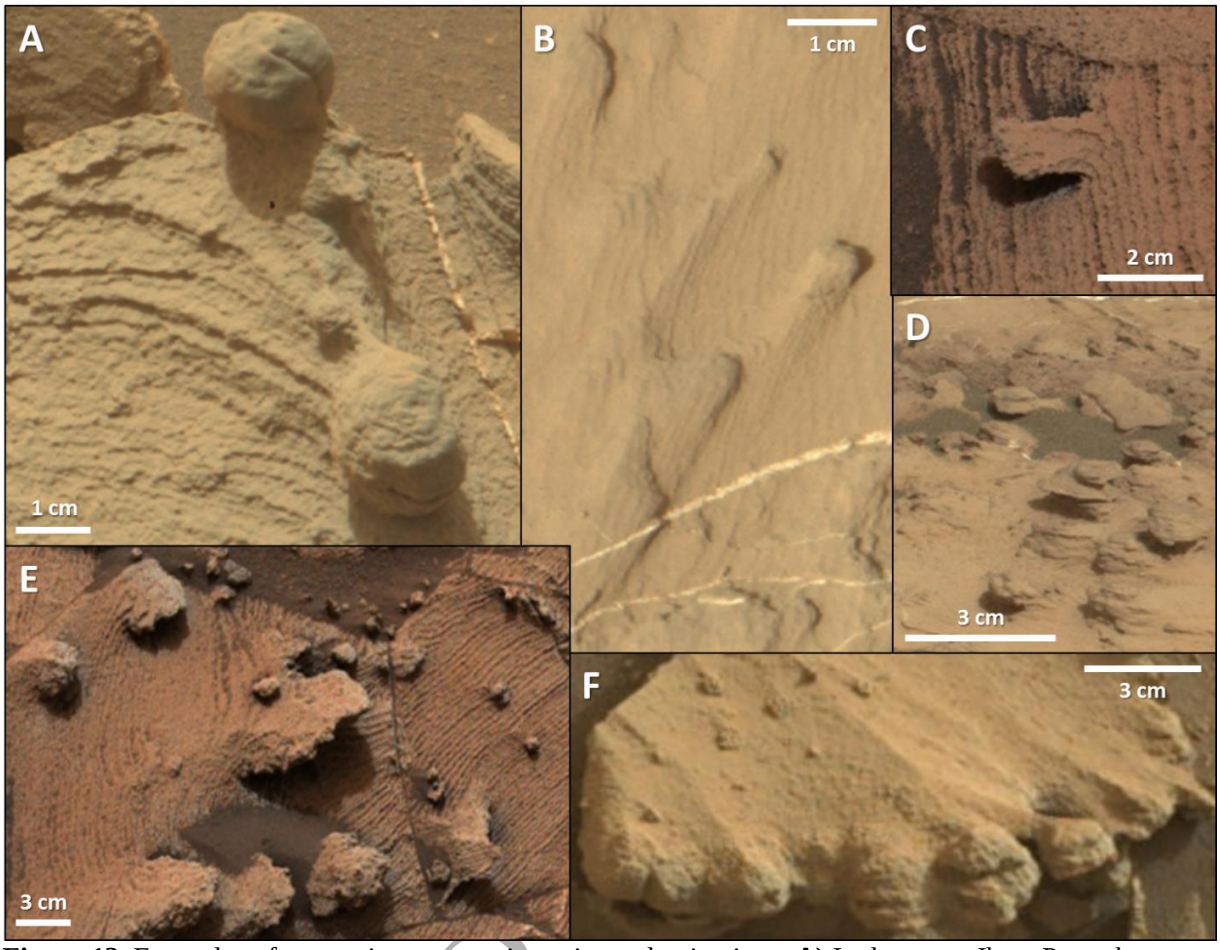

Figure 12. Examples of concretions preserving primary laminations. **A)** In the target Ibex_Pass, the bottom spherical concretion preserves laminations from the surrounding host rock and the top concretion has latitudinal ridges running across the concretion surface (Sol 782, mcam03415). **B)** A plan view of lamination-enhancing features shows the preservation of host rock laminations (Sol 1455, mcam07205). **C)** A cemented knob retains laminations from the surrounding host rock (Crowder on Sol 792, mcam03447). **D)** Smooth irregular concretions have a lensoidal shape, possibly due to preferential cementation along bedding planes (Nokaneng on Sol 1497, mcam07579). **E)** Rough-textured irregular concretions preserve laminations (Sol 792, mcam03455). **F)** Rough-textured quasi-circular concretions seem to be concentrated along a layer and preserve original bedding planes (Sol 780, mcam03405).

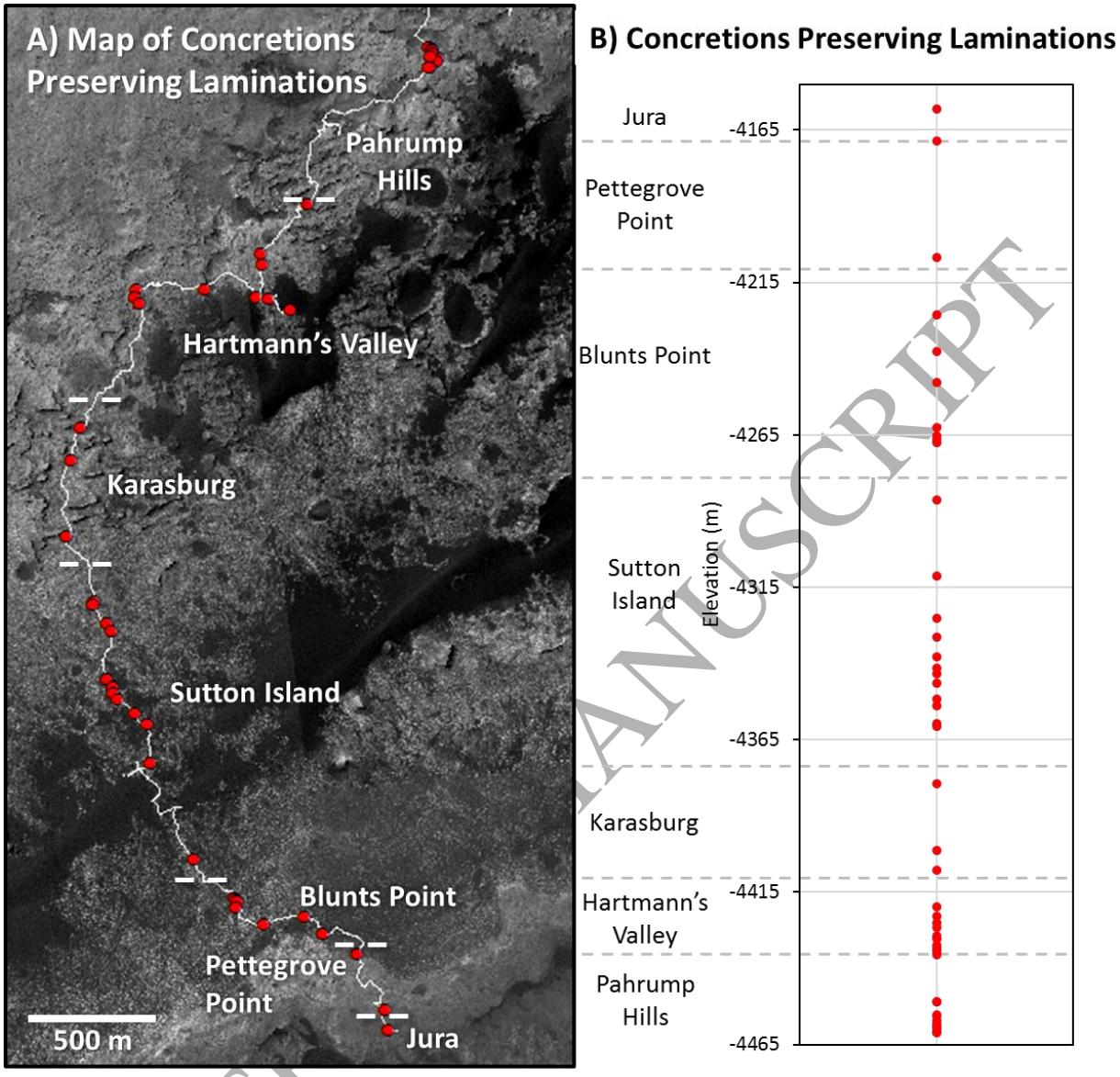

Figure 13. A) Distribution of concretions observed to preserve primary laminations along Curiosity's traverse. **B)** Stratigraphic distribution of concretions preserving primary laminations, with points corresponding to the same points as in A). Each red point represents an individual rover location or elevation where concretions were observed to preserve primary host rock laminations.

4.4 Associations with Other Diagenetic Features

Veins and concretions are the most prevalent diagenetic features observed in the Murray formation and commonly occur together in the same locations throughout almost all of the Murray members **(Figure 14,15)**. For example, diffuse sulfate veins in the Sutton Island and Blunts Point members are dispersed within concretionary bodies **(Figure 14A)**. Concretions may also appear suspended in or enveloped by sulfate veins **(Figure 14B,D)**, and can be crosscut by veins **(Figure 7D, 14C)**; for instance, dendrites in the Pahrump Hills member often are crosscut by small sulfate veins (**Figure 8B**; *Kah et al., 2015*). Antithetical relationships are also observed between concretions and veins, where concretion-dense areas contrast with concretion-free zones

immediately surrounding sulfate veins **(Figure 14E)**. These antithetical associations are primarily observed near the boundary between the Karasburg and Sutton Island members and in the Pettegrove Point member **(Figure 15)**.

Associations between concretions and other diagenetic or mineral alteration features (e.g., alteration halos, crystal molds) are rare and have not been confidently identified in the Murray formation. However, concretions have been observed in association with alteration halos in the Stimson formation and take on a bleached, lighter-toned appearance compared to concretions that occur outside of the halo **(Figure 16)**. Though this example does not occur in the Murray formation, this may serve as a proxy for concretion and alteration halo relationships in the Murray since these halos crosscut both the Murray and Stimson formations. *(Yen et al., 2017; Frydenvang et al., 2017).*

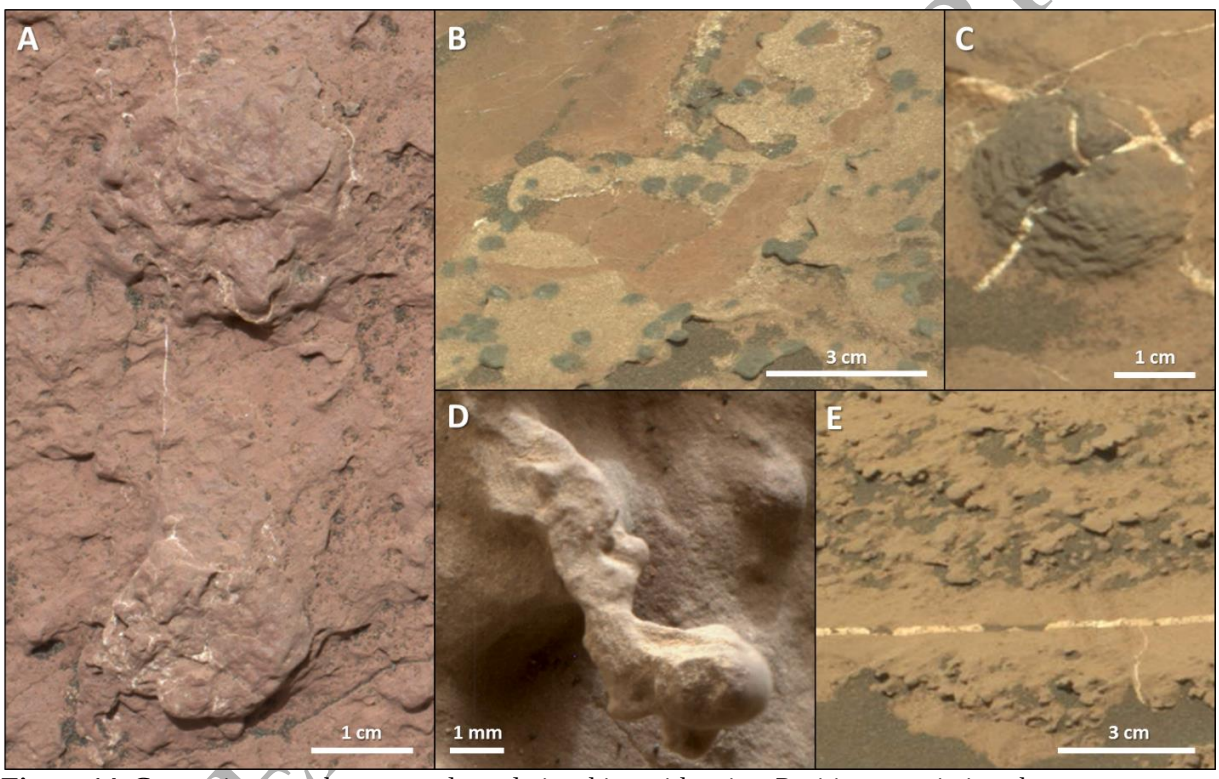

Figure 14. Concretions can have complex relationships with veins. Positive associations between concretions and veins are observed in: **A)** Irregular concretions in Sutton Island, which sometimes have diffuse sulfate veins dispersed throughout the concretion body (Mansell_Mountain on Sol 1577, MAHLI 25 cm standoff), **B)** Concretions that appear suspended in a sulfate sheet (Mosely_Point on Sol 1732, mcam09047), or **D)** Spherules that are enveloped in vein material (Andulo on Sol 1444, MAHLI 2 cm standoff). **C)** The large spherule target Viana is crosscut by veins (Sol 1441, mcam07126). **E)** Antithetical relationships between concretions and veins are observed in the Bonney_Woods target (Sol 1828, mcam09454).

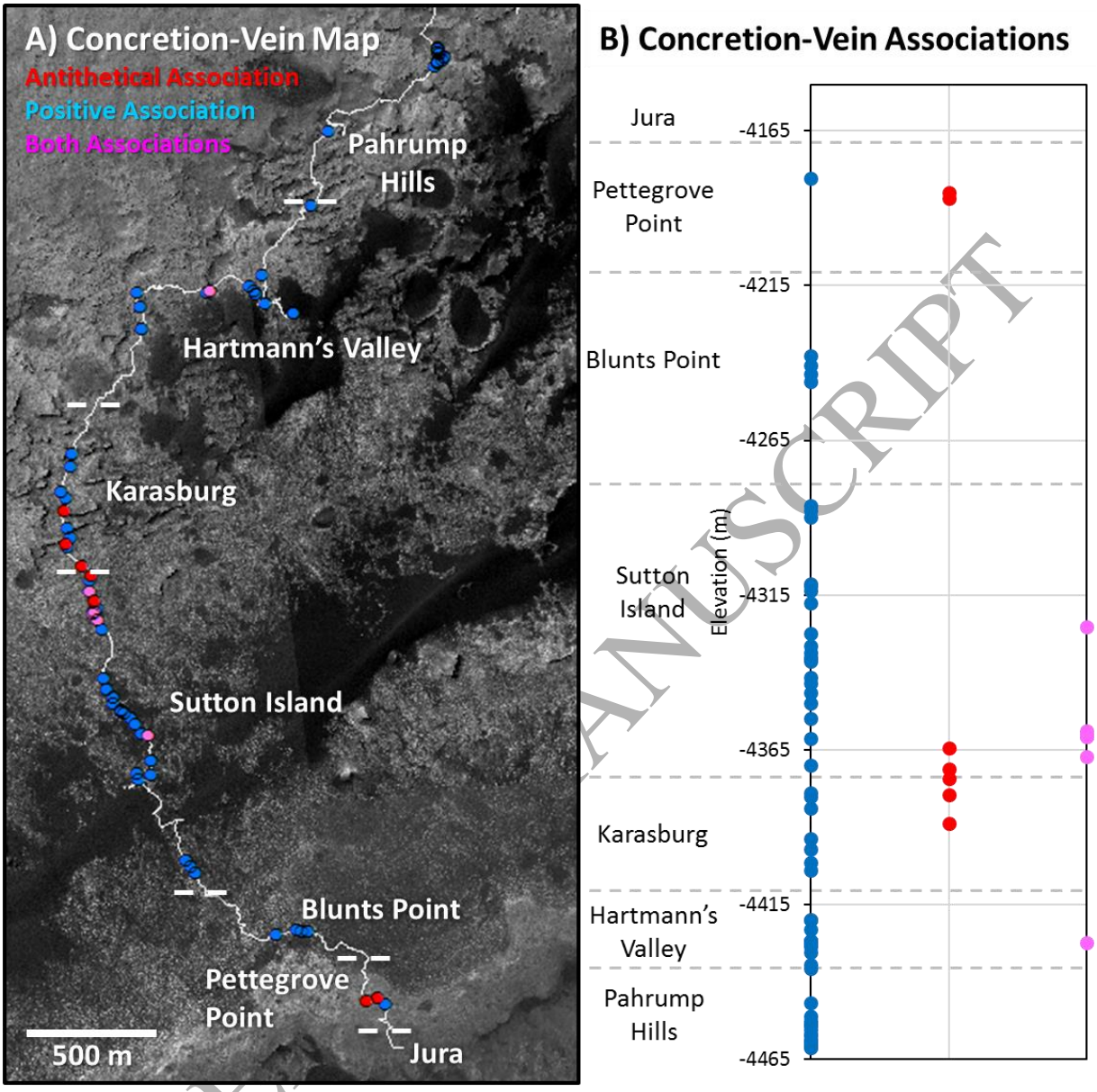

Figure 15. A) Geographic distribution of positive and antithetical associations between concretions and veins, as well as sites where both associations are observed. **B)** Stratigraphic distribution of the various associations between concretions and veins, using the same color scheme as in A).

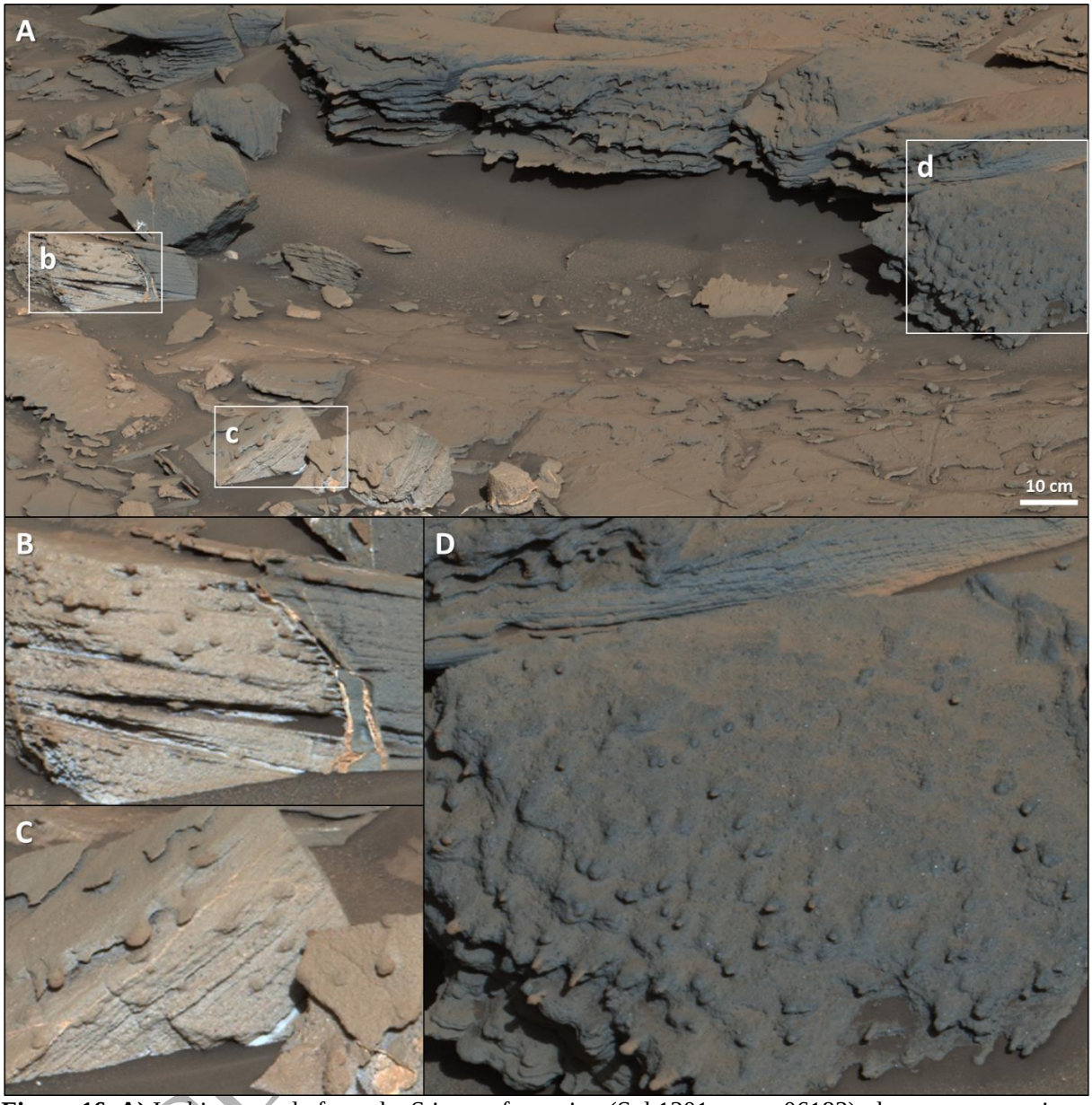

Figure 16. A) In this example from the Stimson formation (Sol 1301, mcam06183), the same concretion morphology appears **B,C)** associated with alteration halos and **D)** without association with alteration halos.

5. Size, Density, and Spacing of Murray Formation Concretions

5.1 Concretion Size and Density

The size of spherules and irregular concretions was systematically measured or approximated, as these two groups were the most common morphologies observed throughout the traverse of the Murray formation.

The size distributions of in situ spherules averages 1.49 ± 0.95 mm but appears to increase upsection through the Murray formation. A systematic survey of 1449 spherule sizes from 50 MAHLI observations **(Table 1, Figure 17)** shows that mean spherule sizes in the Pahrump Hills and Karasburg members are ~1.1 ± 0.6 mm and increase to 1.30 ± 0.62 mm in

Sutton Island, 1.42 ± 0.69 mm in Blunts Point, and 3.55 ± 0.80 mm in Pettegrove Point. Even larger spherules, averaging 4.01 ± 0.98 mm in size, occur in eroded materials of the Gunning_Rocks target in the lower Pettegrove Point member (-4206.4 m elevation), and may represent spherules eroded out from stratigraphically higher members of the Murray formation.

A left-sided Wilcoxon rank sum test was applied to determine if spherule sizes increase upsection between successive Murray members at the 99% significance level **(Table 2)**. The Wilcoxon rank sum test compares two independent populations that are not necessarily normally distributed and tests the null hypothesis (H_0) that the median of the spherule size population is the same between a Murray member and the next stratigraphic member upsection. Results show that spherule size increases between the Karasburg, Sutton Island, Blunts Point, and Pettegrove Point members, at the 99% significance level. There is no significant difference in spherule size between the Pahrump Hills and Karasburg members, nor between the Pettegrove Point member and the Gunning_Rocks eroded material. We note that the Pettegrove Point sample size of 17 is much smaller than for the other members. However, the Pettegrove Point size distribution is still distinct from, and is overall larger than, the distribution of the preceding Blunts Point member, as indicated by the associated p-value.

The size of the irregular concretions was also approximated from Mastcam workspace mosaics throughout Curiosity's traverse **(Figure 18)**, as this morphology exhibits a wider, and generally larger, range of sizes compared to spherules. The maximum spherule concretion size is shown for comparison with the irregular concretions; these Mastcam-based measurements are separate from the aforementioned spherule size distributions derived from MAHLI images **(Figure 17)**. The maximum irregular concretion size tends to decrease upsection in the Murray formation **(Figure 18)**. The largest irregular concretions tend to be in the Pahrump Hills and Hartmann's Valley members and can be larger than 30 mm along their longest axis. The maximum irregular concretion decreases in size to less than 10 mm in the upper half of Sutton Island and Blunts Point, and decreases to even smaller, millimeter-scale sizes in the Pettegrove Point and Jura members. Thus, while small concretions are present at all levels of the Murray formation, these results show that large centimeter-scale concretions are primarily present in the lower Murray fm. and largely absent in the uppermost Murray members.

We also observe a qualitative trend of concretion density (encompassing all concretion morphologies) decreasing upsection in the Murray **(Figure 19)**. While the scenes from any given rover location can be quite variable, the lower portions of the Murray formation in Pahrump Hills, Hartmann's Valley, and Karasburg tend to have more locations where high concretion density is observed. In contrast, the upper Murray members, including Sutton Island, Blunts Point, Pettegrove Point, and Jura, have fewer locations where high concretion density is observed.

Murray Member	N	Average Size (mm)	Standard Dev. (mm)	Median Size (mm)	Minimum Size (mm)	Maximum Size (mm)
Pahrump Hills	36	1.10	0.60	1.02	0.32	2.53
Karasburg	149	1.11	0.65	0.94	0.30	4.58
Sutton Island	773	1.30	0.62	1.15	0.38	5.62
Blunts Point	389	1.42	0.69	1.25	0.48	4.98
Pettegrove Point	17	3.55	0.80	3.84	1.42	4.66
Gunning_Rocks (Float)	85	4.01	0.98	3.97	2.11	6.53

All	1449	1.49	0.95	1.20	0.30	6.53

Table 1. Statistics for spherule sizes measured from MAHLI images. Results are grouped by Murray member, except for the Gunning_Rocks observation of a collection of float spherules. These measurements represent the longest dimension of the spherules, as some spherules are sub-spherical.

Compared Datasets	***p***	**Reject H_0 ?**
Pahrump Hills vs. Karasburg	0.50	No
Karasburg vs. Sutton Island	4.36E-08	Yes
Sutton Island vs. Blunts Point	2.54E-04	Yes
Blunts Point vs. Pettegrove Point	8.56E-11	Yes
Pettegrove Point vs. Gunning_Rocks (Float)	0.08	No

Table 2. Wilcoxon rank sum testing results comparing if spherule size populations increase upsection between successive Murray members at the 99% significance level. The null hypothesis (H_0) is that the median of the spherule size population is the same between a Murray member and the next stratigraphic member upsection.

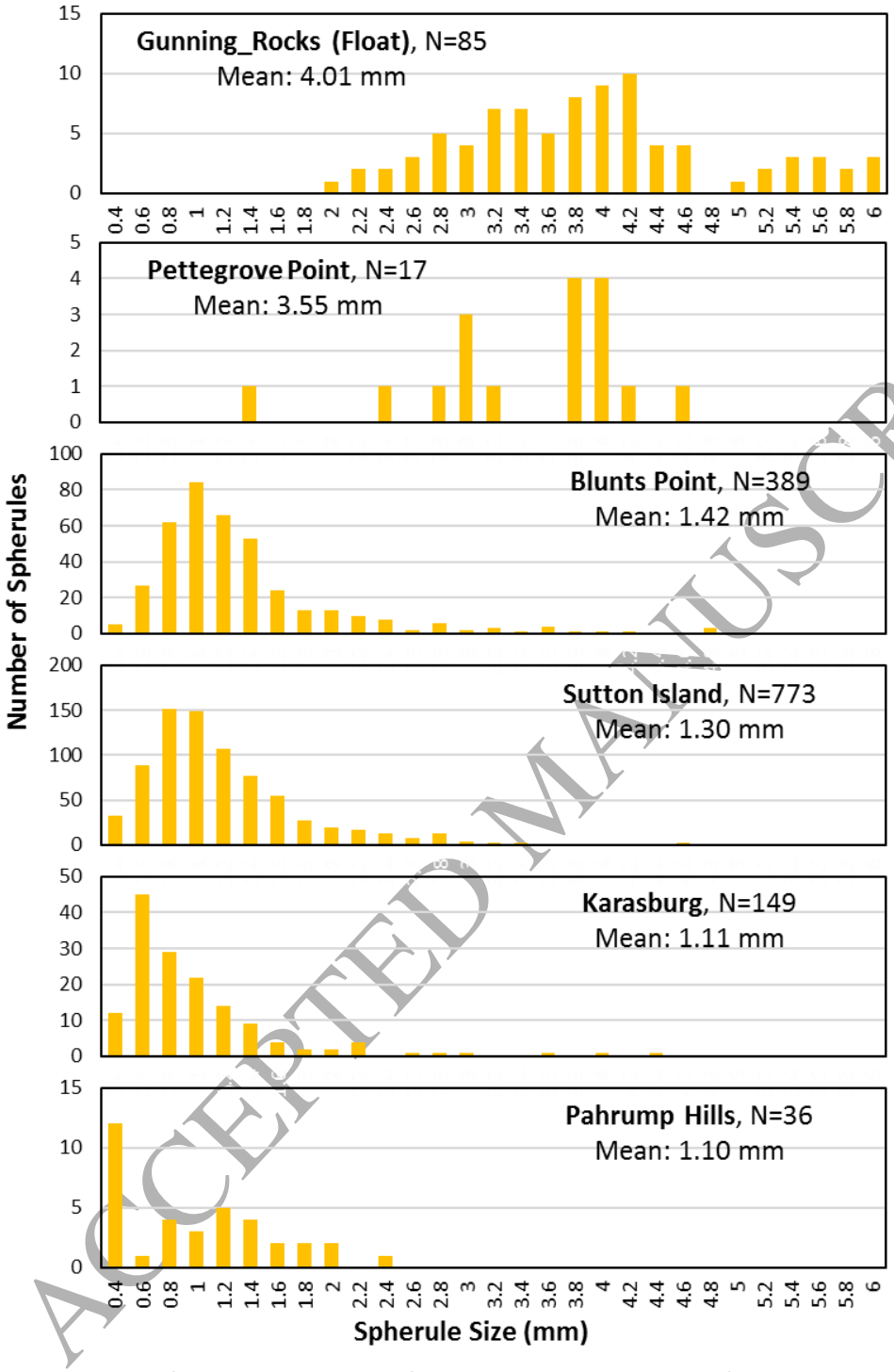

Figure 17. Size frequency histograms for 1449 spherules measured from MAHLI observations of 50 targets throughout the Murray formation. Results are grouped by Murray member, except for the Gunning_Rocks observation of a collection of float spherules. Hartmann's Valley and Jura are not represented here due to lack of data. Please see **Table 2** for the statistical interpretations of these distributions.

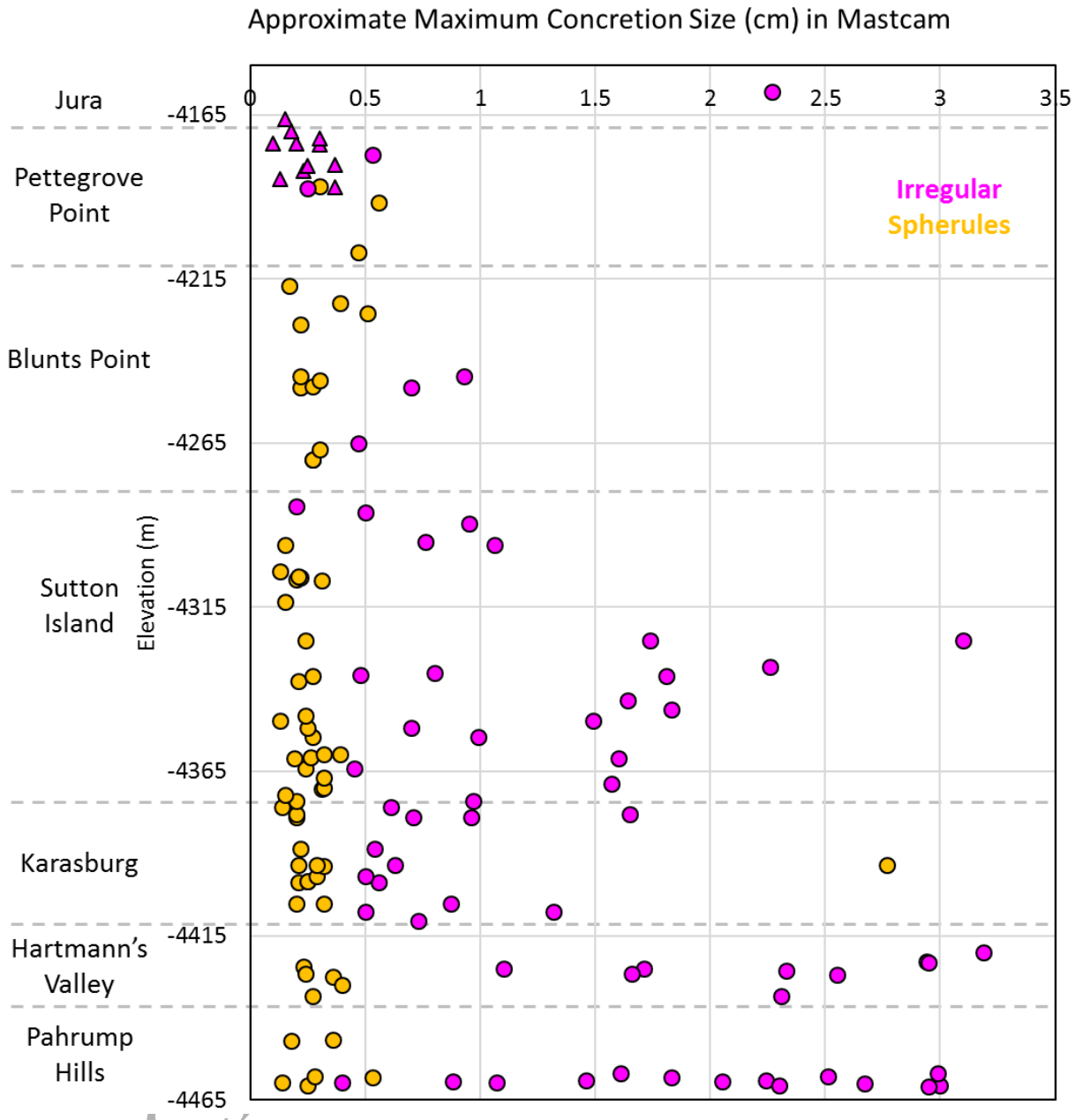

Figure 18. Apparent maximum size of irregular concretions, measured from a representative set of 124 Mastcam workspace images (circles) and 11 MAHLI images (triangles) where the largest visible concretions were too small to resolve in Mastcam images in the Pettegrove Point and Jura members. The apparent maximum size of spherules is shown for comparison; these spherule measurements complement the more detailed size distributions derived from a separate set of MAHLI images **(Figure 17)**. Please note that the data in this plot are meant to be interpreted qualitatively to illustrate the upsection decrease in concretion size.

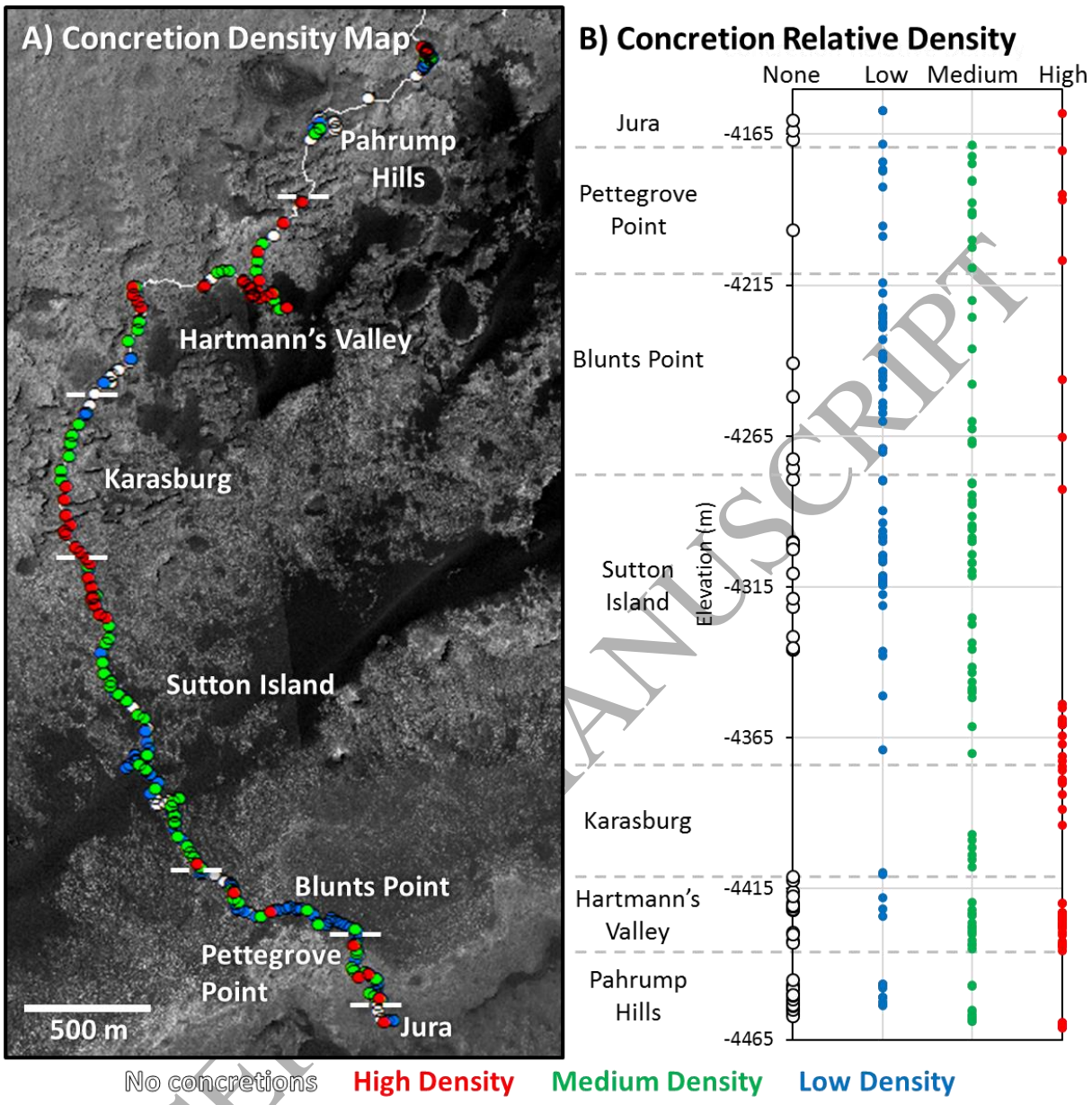

Figure 19. A) Distribution of concretion density, as determined from qualitative estimation **(Figure 3)**, along Curiosity's traverse. **B)** Stratigraphic distribution of relative concretion density, with points corresponding to the same points as in A). Each point represents an individual rover location or elevation, with colors corresponding to an absence of concretions or concretions present at low, medium, or high density.

5.2 Spherule Spacing

The degree of clustering between spherules was assessed from average nearest neighbor (ANN) statistics calculations performed for 44 MAHLI targets that contained multiple spherules in an image scene **(Table 3)**. The Nearest Neighbor (NN) ratio is less than one and indicates clustering for spherules in 34 targets. Ten targets have NN ratios greater than one, indicating that spherules in those targets are dispersed. The plot of spherule size against the observed ANN

distance suggests that smaller spherules are more closely spaced whereas larger spherules are more widely spaced **(Figure 20)**.

Target	El (m)	N	Average Size (mm)	Size SD (mm)	Obs. ANN Dist. (mm)	ANN SD (mm)	Exp. ANN Dist. (mm)	Nearest Neighbor Ratio	P value
Ricardo	-4460.7	18	0.68	0.38	4.17	2.33	4.98	**0.84**	0.19
Morrison	-4460.45	18	1.52	0.49	4.79	4.09	12.62	**0.38**	0
Conda	-4398.41	6	2.37	1.56	8.38	1.36	8.63	**0.97**	0.89
Andulo	-4393.47	38	0.93	0.39	3.29	1.45	3.43	**0.96**	0.62
Ganda	-4393.46	46	0.98	0.42	2.77	2.15	3.16	**0.88**	0.11
Quela	-4379.56	22	1.3	0.59	4.58	1.96	4.66	**0.98**	0.87
Ombomboli	-4379.25	19	1.16	0.92	5.9	4.48	5	**1.18**	0.13
Serowe	-4363.93	78	1.1	0.33	5.65	5.64	7.85	**0.72**	0
Thrumcap	-4351.53	223	1.17	0.67	3.93	2.71	4.64	**0.85**	0
Pemetic	-4349.6	43	1.02	0.21	9.46	6.49	10.58	**0.89**	0.18
Mansell_Mountain	-4335.75	30	1.35	0.34	14.45	11.79	12.69	**1.14**	0.15
Mars_Hill and Camera_Hill	-4324.84	16	0.88	0.25	5.79	4.69	6.91	**0.84**	0.21
Bluffer_Pond	-4317.29	38	1.05	0.21	4.98	5.9	7.92	**0.63**	0
Cape_Elizabeth	-4314.01	14	1.69	0.26	16.6	19.45	17.29	**0.96**	0.77
Spurwink	-4313.17	88	0.9	0.31	4.86	3.45	6.51	**0.75**	0
Passagassawakeag	-4313.07	8	0.85	0.25	6.23	6.79	7.77	**0.8**	0.28
Whiskey	-4312.22	90	1.39	0.3	5.24	4.45	7.33	**0.72**	0
Digdeguash	-4311.18	6	2.84	0.53	18.38	11.72	28.32	**0.65**	0.1
Munsungun	-4311.06	22	1.48	0.39	16.42	11.46	14.82	**1.11**	0.33
Misery	-4310.81	14	1.58	0.44	20.1	13.9	18.53	**1.08**	0.54
Spider_Lake	-4306.53	58	2.43	0.44	7.65	6.23	9.1	**0.84**	0.02
Maple_Spring	-4289.43	10	1.3	0.52	18.64	27.98	21.91	**0.85**	0.37
Ikes_Point	-4279.16	5	0.88	0.2	12.74	5.4	9.94	**1.28**	0.23
Fern_Spring	-4270.07	11	2.87	0.69	25.59	12.73	20.88	**1.23**	0.15
Frazer_Creek	-4247.77	16	1.59	0.57	14.02	8.27	17.33	**0.81**	0.14
Lurvey_Spring	-4247.75	6	1.68	0.41	37.91	15.68	28.26	**1.34**	0.11
Pierce_Head	-4247.13	5	1.4	0.35	24.01	13.27	29.89	**0.8**	0.4
McFarland_Mountain	-4246.21	16	1.63	0.58	6.37	15.19	17.28	**0.37**	0
Pecks_Point	-4246.18	12	1.52	0.2	9.37	17.36	19.97	**0.47**	0
Winter_Harbor	-4246.14	18	2.01	0.61	15.77	19.67	16.34	**0.97**	0.78
Jobbies	-4243.07	47	1.04	0.58	3.94	8.68	9.13	**0.43**	0
Appledore	-4240.4	2	0.89	0.09	30.6	0	15	**2.04**	0
Tupper_Ledge	-4239.03	19	1.02	0.28	8.38	12.29	15.89	**0.53**	0

Foxbird	-4237.4	8	2.83	1.59	17.18	10.42	22.06	**0.78**	0.23
Dumplings Island 1	-4227.25	76	1.34	0.35	8.08	18.11	11.75	**0.69**	0
Dumplings Island 2	-4227.25	35	1.26	0.44	5.68	5.79	7.95	**0.71**	0
Pond of Tea	-4227.25	3	1	0.22	17.54	12.86	22.14	**0.79**	0.29
Thorne	-4227.25	7	2.58	2.08	28.32	15.58	34.32	**0.83**	0.56
Burnt Coat	-4227.25	17	1.23	0.83	14.05	10.95	13.7	**1.03**	0.84
Emery Cove	-4225.94	21	1.58	0.61	8.88	13.92	15.16	**0.59**	0
Agamenticus	-4222.52	8	1.68	0.71	10.96	20.47	24.26	**0.45**	0
Doliver	-4217.47	56	1.32	0.36	4.28	5.09	7.83	**0.55**	0
Bauneg Beg	-4214.21	13	3.41	0.81	18.51	12.07	19.2	**0.96**	0.8
Robinson Rock	-4206.88	4	4.02	0.63	34.03	47.99	33.31	**1.02**	0.93

Table 3. Average nearest neighbor (ANN) statistics for 44 individual MAHLI targets, in order of increasing elevation. In order, columns indicate the target name, elevation (m), number of spherules, average spherule size (mm), size standard deviation (mm), observed ANN distance (mm), ANN standard deviation (mm), expected ANN distance (mm), the nearest neighbor (NN) ratio, and the p value. Red NN ratios indicate that the spherules are clustered and blue NN ratios indicate that the spherules are dispersed.

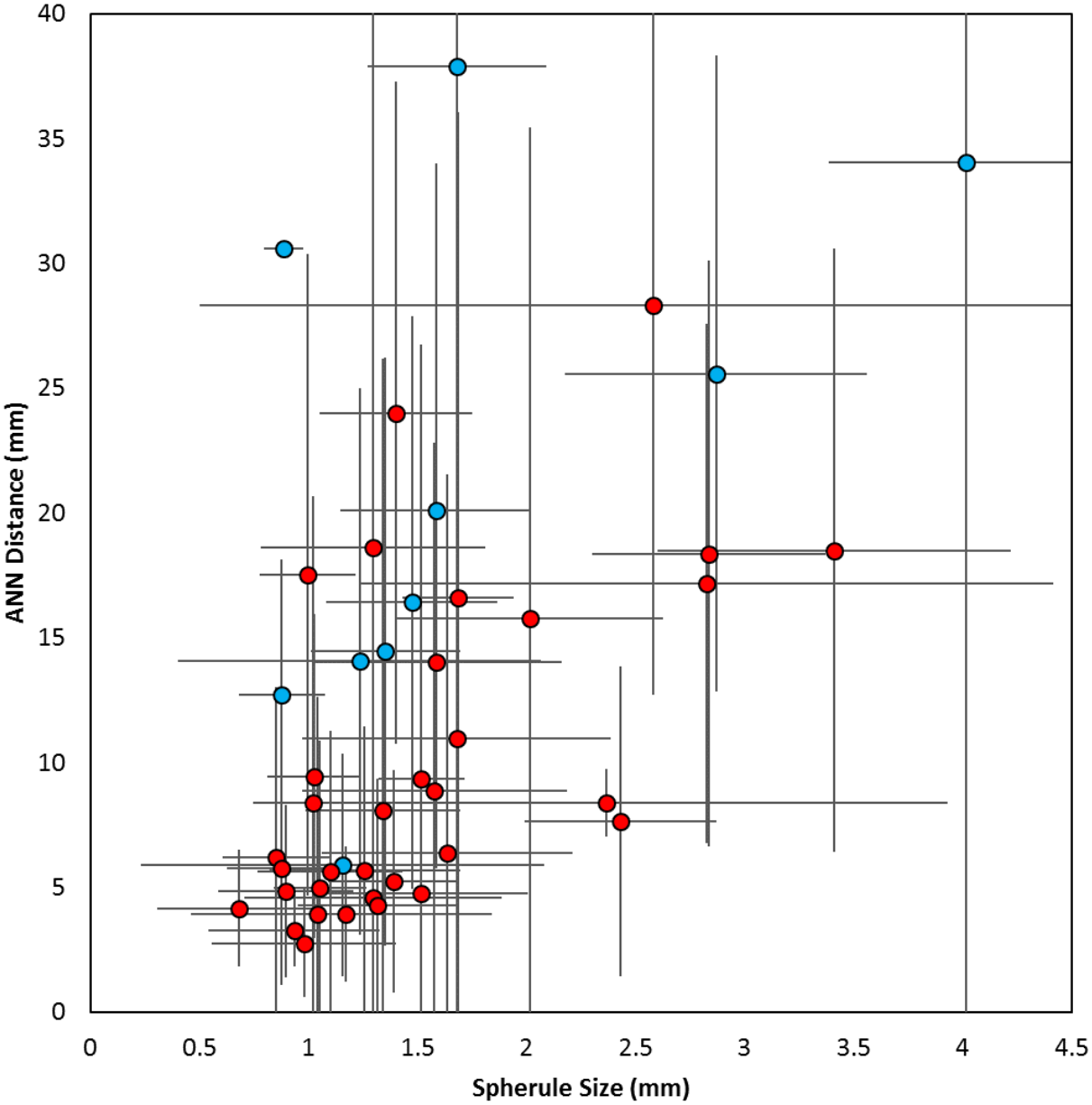

Figure 20. Distribution of spherule size and average nearest neighbor (ANN) distance in the 44 MAHLI targets from **Table 3**. Error bars are standard deviations of the size and ANN distance measurements. Red corresponds to MAHLI targets with clustered spherules and blue corresponds to targets with dispersed spherules, as indicated by the nearest neighbor ratio **(Table 3)**.

6. Chemistry of Murray Formation Concretions

APXS and ChemCam-derived compositions show that different concretion morphologies are not uniquely correlated with elemental enrichments. Instead, there are at least three distinct stratigraphic intervals where elemental enrichments in concretion-rich targets correspond with certain concretion assemblages.

At the base of the Pahrump Hills member (elevation -4460 m), dendrites, irregular concretions, and other raised, resistant diagenetic features are enriched in Mg, S, and Ni, as well as Cl (**Figure 21A**, *Thompson et al., 2015, Nachon et al., 2016*). These enrichments are consistent with the addition of a ~11% cement dominated by a Mg-, Ni, and S-bearing phase or phases (*VanBommel et al., 2016*). ChemCam detected up to three times the host rock MgO content and up to 15% MgO, interpreted to represent Mg-sulfate (**Supporting Figure 1**, *Nachon et al., 2016*).

Concretions encountered between -4305 and -4250 m elevation within the upper Sutton Island and Blunt's Point members, which predominantly include flat and some irregular morphologies, typically exhibit Mn and P enrichments in the APXS data, up to 14 and 6.5 times the background bedrock concentrations respectively **(Figure 21B)**. Manganese and P enrichment is variously accompanied by enhanced concentrations in Fe, Mg, and Zn (*Thompson et al., 2017*). Some enrichments in Ca and S are also variably observed, suggesting contributions from Ca-sulfate materials in the APXS FOV. A few of these targets show substantial Fe enrichment as well, up to 1.9 times the bedrock concentration. ChemCam observations also show similar enrichments in Fe, Mg, Mn, and P in flat concretionary features in this stratigraphic interval (**Supporting Figure 1**, *Gasda et al., 2018; Meslin et al., 2018; Lamm et al., 2018*), and compositional variations may correspond to different textures within this flat concretion group (*Meslin et al., 2018*). Within this elevation range, a number of APXS targets containing flat concretions in the Blunts Point member also show enrichments only in Ca and S **(Figure 21B)**, suggesting either the presence of Ca-sulfate in these concretions or reflecting the abundance of layer-parallel and subparallel Ca-sulfate in the local strata (*Fedo et al., 2018*).

APXS observations also reveal other, more isolated, elemental enrichments that are not widespread within the Murray formation. At -4352 m elevation in the Sutton Island member, the Thrumcap halo feature exhibits elevated K concentration at 2.5 times the adjacent Murray bedrock and slightly elevated Fe and S (*Yen et al., 2018*). Concretion and bedrock targets near Thrumcap exhibit similar enrichments in K and Fe, the latter up to 1.6 times the nearby concretion-free bedrock at the same elevation **(Figure 21C)**. Putative desiccation cracks were observed at the Old_Soaker target at -4336 m in Sutton Island (*Stein et al., 2018*), and concretions and bedrock in this area exhibit Na and Cl concentrations elevated over nearby Murray host rock **(Figure 21D)**. The Gunning_Rocks float spherules, in the basal Pettegrove Point member (**Figure 4C-E**; -4206 m elevation), show substantial enrichment in Mg, Mn, P, Fe and Zn relative to all other targets at that elevation **(Figure 21E)**.

A number of concretion-bearing targets revealed no marked change in composition relative to nearby bedrock targets, for example much of the Hartmann's Valley and Karasburg members **(Figure 21)**. This may be a consequence of the APXS FOV not including the features of interest, the minor contribution of the concretionary features to the APXS FOV (and therefore signal), or no substantial difference in chemistry between the concretion and local bedrock **(Section 3.2)**.

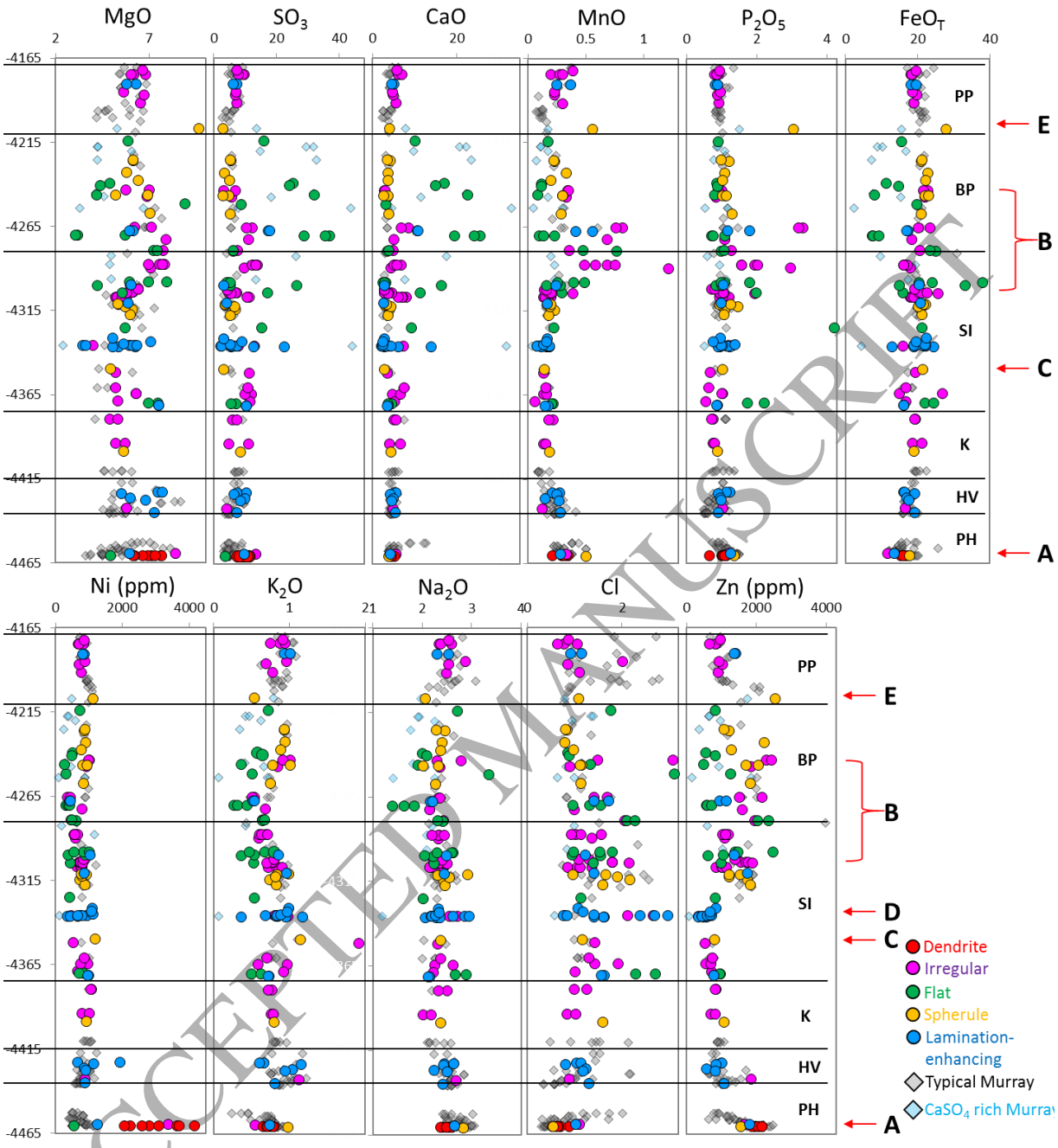

Figure 21. APXS compositions of concretion-rich targets (circles colored by concretion morphology) and, for comparison, typical Murray (grey diamonds) and Ca-sulfate-rich Murray (blue diamonds). Letters correspond to six intervals where distinct concretion enrichments are observed. **A)** Mg, S, and Ni enrichments at the base of Pahrump Hills (-4460 m elevation). **B)** Mn and P enrichments and varying Fe, Mg, Ca, S, and Zn enhancements within the upper Sutton Island and Blunts Point members (-4305 to -4250 m elevation). Note that even higher Mn and P is observed but not indicated in this plot. Several concretion-rich targets in this interval of Blunts Point are enriched only in Ca and S. **C)** Local enrichments in K, Fe, and S near the Thrumcap target at -4352 m elevation in Sutton Island. **D)** Local enrichments in Na and Cl near the Old_Soaker target at -4336 m elevation in Sutton Island. **E)** Mg, Mn, P, Fe, and Zn enrichments in the Gunning_Rocks float spherules at -4206 m elevation in Pettegrove Point.

PH = Pahrump Hills, HV = Hartmann's Valley, K = Karasburg, SI = Sutton Island, BP = Blunts Point, PP = Pettegrove Point, J = Jura.

7. Constraining Formation Conditions of the Murray Concretions

The assembled observations of concretion shape **(Sections 4.1, 4.2)**, size **(Section 5)**, chemistry **(Section 6)**, and associations with other diagenetic features and host rock **(Sections 4.3, 4.4)** can inform about host rock properties and fluid chemistries at the time of concretion formation in the Murray formation.

7.1 Interpretation of Growth Mechanisms

Concretion morphologies result from a variety of growth mechanisms and host rock and fluid flow properties. The spherical shape of Murray spherules reflects their formation in isotropic conditions with similar porosity and permeability and a lack of directional fluid flow in all three dimensions (e.g., *Berner, 1968; Chan et al., 2005; Potter et al., 2011*). For example, terrestrial spherules are more likely to grow in isotropic sediments like sand and fresh mud (e.g., *Bowen et al., 2008; Marshall and Pirrie, 2013*), and previously identified martian spherules at Meridiani Planum and in the Yellowknife Bay formation at Gale crater were interpreted to have formed in the presence of stagnant groundwater (*McLennan et al., 2005; Calvin et al., 2008; Stack et al., 2014*). More irregular concretion morphologies in the Murray formation can result from multiple fluid histories (e.g., *Minitti et al., 2018*), or formation in heterogeneous conditions when porosity, permeability, and fluid flow vary in the host sediment or rock (*Potter-McIntyre et al., 2014*). We note that we do not observe elongate concretions, which have orientations that are suggestive of strong directional fluid flow (*McBride et al., 1999*).

Flat concretions in the Murray formation share morphologic characteristics with some terrestrial concretions (typically carbonate, e.g., "nodular limestone," or chert), which can have flattened and ellipsoidal shapes that sometimes coalesce to form lateral layers that extend for a few meters (e.g., *Pearson, 1979; Pye, 1981; McBride and Parea, 2001; Fischer and Knoll, 2009*). On Earth, these flat concretions likely formed from precipitation along a particular stratigraphic horizon with preferential cementation exploiting permeability within a given horizon (*Coleman, 1993; Potter-McIntyre et al., 2014*), a phenomenon that is especially common in fine-grained sediments (*Oertel and Curtis, 1972*). This tendency may explain the prevalence of flat concretions in the Karasburg, Sutton Island, and Blunts Point members **(Figure 11C)**, which contain the highest proportion of clay minerals (up to ~35 wt%) observed in the Murray formation by the CheMin instrument (*Rampe et al., 2017*). Alternatively, it has been proposed that these flat concretions, which tend to be enriched in Fe and Mn, may have formed syndepositionally or during early diagenesis at the water-sediment interface under shallow and oxidizing lacustrine conditions (*Meslin et al., 2018*).

Other morphologies represent more specific formation conditions. The dendrites at Pahrump Hills are defined by their branching nature, which reflects mineral precipitation from hypersaturated fluids as two or more chemically distinct pore fluids mix (*Seilacher, 2001; Kah et al., 2015; Minitti et al., 2018*). Lamination-enhancing features lack boundaries that distinguish them from the host rock, suggesting that they have less cement and a larger component of host rock grains compared to discrete concretions. Such features could indicate lesser amounts of cementing agents present in diagenetic fluids or mild changes in environmental conditions that induced a lesser degree of concentrated cementation.

The Murray concretions could have grown through either concentric or pervasive growth, or some combination of both processes (*Raiswell and Fisher, 2000*), though the exact

mechanism is difficult to identify with Curiosity's payload (*Stack et al., 2014*). During concentric growth, the concretion body accretes outwards as layers of pore-filling cement precipitate around a nucleus (e.g., *Mozley, 1996*). At the scale of Mastcam and MAHLI images, none of the in situ Murray concretions exhibit internal layering that is characteristic of concentric growth, though this does not preclude growth by this process. We note that internal structures were observed in concretions in the Yellowknife Bay formation (*Grotzinger et al., 2014; Stack et al., 2014; Wiens et al., 2017*), but are rare in the 300 meters of traversed Murray formation **(Figure 5)**. During pervasive growth, mineral cement precipitates through a region of sediment pore spaces, and the resulting concretion often forms from multiple precipitation events (e.g., *Raiswell and Fisher, 2000; Potter et al., 2011*). Pervasive growth is a plausible formation mechanism for some of the Murray concretions, particularly for concretions that are not substantially compositionally different from the host rock **(Figure 21)**, as the initial stages of pervasive growth involve lesser amounts of cement (*Raiswell and Fisher, 2000; Stack et al., 2014*). Lastly, nearest neighbor analyses of spherules **(Section 5.2)** show that smaller spherules may be more closely spaced compared to larger spherules suggesting self-organized spherule formation where equal amounts of precipitated solute are added to the growing concretion surfaces (cf. *Chan et al., 2004; Potter and Chan, 2011; Potter et al., 2011*).

7.2 Timing of Diagenesis

The timing of concretion formation relative to sediment deposition, burial, and lithification can be constrained by assessing the association of concretions with primary host rock laminations and other diagenetic features. A number of Murray concretions are observed to preserve primary host rock laminations, and there is no evidence for warped or deflected laminae at the boundary between the concretion and host rock **(Section 4.3)**, a feature known as "differential compaction" (e.g., *Raiswell, 1988; Lash and Blood, 2004*). Differential compaction occurs when concretions form prior to sediment compaction and lithification, when sediments are unconsolidated and host substantial porosity (e.g., up to >80% in mudstones; *Day-Stirrat et al., 2012*) that can be occluded by concretion formation. During sediment burial, concretions are relatively resistant to compaction and cause the surrounding sedimentary laminae to deflect around the concretion, resulting in differential compaction. The preservation of primary host rock laminae in many Murray concretions and lack of evidence for differential compaction **(Figure 12)** is therefore conclusive evidence that a number of concretions formed during late diagenesis after sediment compaction and lithification.

Certain concretion morphologies can also be explained by a late diagenetic origin. The bedding-parallel nature of many flat concretions **(Figure 6)** could have resulted from formation along permeable bedding planes during later diagenesis (e.g., *Coleman, 1993*), although syndepositional or early diagenetic origins have also been proposed for these flat features (*Meslin et al., 2018*). The Pahrump Hills dendrites are often associated with fractures and likely formed during late diagenesis (*Kah et al., 2015; Minitti et al., 2018*). Lamination-enhancing features likely contain less cement and more host rock material **(Section 7.1)**, suggesting that these features formed after substantial sediment compaction when there was less porosity available for the cement to fill; this is also suggested by the preservation of primary laminations, without evidence for differential compaction, in some lamination-enhancing features **(Figure 12B)**.

The upsection decrease in the maximum Murray concretion size **(Figure 18)** and density **(Figure 19)** may reflect a corresponding decrease in porosity and permeability, suggesting late

diagenetic concretion formation after earlier cementation events in the upper Murray formation. On Earth, low porosity and permeability results in smaller and more sparsely distributed concretions (*Chan et al., 2005*), and the small concretion sizes observed at Yellowknife Bay were interpreted to suggest limited fluid transport or diffusion reflecting the low permeability of the clay-rich Sheepbed mudstone (*Stack et al., 2014*). The relatively higher clay content in the upper Murray members (*Rampe et al., 2017*) may also have contributed to the trend of concretion size decreasing upsection. The occurrence of the smallest concretions in the Vera Rubin Ridge-forming members, Pettegrove Point and Jura **(Figure 18)**, is consistent with the indurated nature and inferred lower porosity and permeability of these ridge-forming rocks (*Fraeman et al., 2016*) and suggests that concretion formation postdated the initial cementation and loss of porosity in the Jura member. A late diagenetic origin in this scenario is also supported by the preservation of primary laminations in some concretions in the Jura member **(Figure 7F)**.

Finally, the associations between concretions and other diagenetic features also constrain the timing of concretion formation. Examples where veins clearly crosscut concretionary bodies indicate vein formation postdating concretion formation **(Figure 7D, 14C)**. In more ambiguous scenarios where concretions and veins are co-occurring **(Figure 14A,B,D)**, concretions could have either formed after the veins or been engulfed by subsequently formed veins. Antithetical associations between concretions and veins could suggest concretion formation either predating or postdating vein formation **(Figure 14E)**. In the first case, vein-forming fluids could dissolve pre-existing concretions and produce a concretion-free margin around the sulfate vein. In the latter case, initial vein formation could have created an impermeable zone around the vein that would preclude future concretion formation. Although concretions have not been observed in association with alteration halos in the Murray formation, observations from the Stimson formation can be used as an analog, as the alteration halos crosscut both formations. The presence of similar concretion populations within and outside alteration halos in the Stimson formation **(Figure 16)** suggests that concretion formation predates halo formation in both the Murray and Stimson formations.

7.3 Episodicity of Concretion-Forming Events

The wide variety of concretion morphology, size, and composition throughout 300 meters of stratigraphy are a testament to the rich history of post-depositional mineralization tied to pore fluids in the Murray formation. Given the diverse interactions between concretions and other diagenetic features **(Section 4.4)**, as well as evidence for multiple fluid episodes from studies of other diagenetic features and chemistry **(Section 8)**, it is most likely that diagenetic and concretion-forming processes at Gale were widespread and recurring.

Multiple concretion-forming fluid episodes are suggested by the association of distinct chemical enrichments with certain concretion assemblages at specific stratigraphic intervals: 1) Mg-sulfate with Ni and Cl enrichments in dendrites and irregular concretions at Pahrump Hills (*Nachon et al. 2016*), 2) Mn and P enrichments in flat and irregular concretions at Sutton Island and Blunts Point, 3) Ca and S enrichments coinciding with flat concretions and Ca-sulfate veins at Blunts Point, and 4) several other localized enrichments in K, Fe, Na, and Cl **(Section 6; Figure 21)**. The identification of more than three major chemistry groups associated with concretions suggests that there were at least three aqueous events with different fluid compositions interacting with the Murray sediments (e.g., *Thompson et al., 2017; VanBommel et al., 2017*). Though it is possible for a single fluid event to simultaneously form different concretion morphologies (cf. *Chan et al., 2000; Gasparatos, 2012*) due to local variations in

porosity and permeability variations in mudstones (*Huggett, 1993*), the presence of different and distinct elemental enrichments throughout the Murray concretions suggests that multiple fluid episodes of different fluid compositions were involved.

Multiple diagenetic episodes are also suggested by observations of different size distributions of spherules **(Figure 17)** and irregular concretions **(Figure 18)**, as studies of terrestrial concretions have shown that two or more size fractions can correspond to different precipitation events (*Potter et al., 2011; Potter and Chan, 2011*). Complex relationships between concretions and veins also suggest that concretion formation may predate or postdate vein formation throughout different sections of the Murray formation **(Sections 4.4, 7.2; Figure 14)** and point to multiple fluid events rather than a single diagenetic episode at Gale crater.

8. Synthesis: Diagenetic History of the Murray Formation

Placing these concretion observations in the context of the numerous studies of the diagenetic features in the Murray formation enables a reconstruction of the relative timing of diagenetic and depositional events at Gale crater **(Figure 22)**.

As the Pahrump Hills sediments were deposited, crystal laths, inferred to be gypsum crystals on the basis of their lenticular morphology, likely formed syndepositionally (**Figure 22A**; *Grotzinger et al., 2015; Schieber et al., 2015; Martin et al., 2017; Kah et al., 2018***)**. The succeeding Murray members were then deposited, in the order of the Hartmann's Valley, Karasburg, Sutton Island, Blunts Point, Pettegrove Point, and Jura sediments **(Figure 22B)**. During or after the deposition of the Pettegrove Point and Jura sediments, and before substantial concretion formation, an early fluid event resulted in the initial cementation and loss of porosity in these Vera Rubin Ridge members **(Section 7.2; Figure 22C)**.

The precise timing of the formation of specific concretion assemblages is difficult to identify in this depositional timeline based on our current observations. However, there is evidence for late diagenetic concretion formation in all of the Murray members **(Figure 13; Figure 22D)**, allowing constraints to be placed on late stage fluid chemistry as chemical enrichments are associated with late-diagenetic concretion assemblages **(Figure 21)**. At some point after the deposition, burial, and compaction of the basal Pahrump Hills sediments, a Mg-S-Ni-Cl-enriched fluid formed dendrites and irregular concretions (*Kah et al., 2015; Nachon et al., 2016; Minitti et al., 2018*). The formation of spherules and irregular concretions in Hartmann's Valley and Karasburg also occurred after their respective host sediments were compacted and lithified. The formation of flat concretions enriched in Mn, P, and variable Fe and Mg, in the Sutton Island and Blunts Point members may have also occurred after sediment compaction, based on their parallel to subparallel occurrence with primary bedding planes **(Figure 6)**. However, it has also been suggested that these features formed during sediment deposition or during early diagenesis in a shallow, oxidizing lacustrine environment (*Meslin et al., 2018; Gasda et al., 2018; Rapin et al., 2018*). A Ca- and S-enriched fluid may have resulted in the formation of concretions in an overlapping interval of Blunts Point or are related to the formation of some Ca-sulfate veins that are pervasive throughout the Murray formation.

Prior to the unconformable emplacement of the Stimson formation over the Murray formation **(Figure 22E)**, multiple generations of veins had formed in the Murray formation **(Figure 22G)**, suggested by various chemical enrichments in veins (e.g., *Nachon et al., 2016; L'Haridon et al., 2018*) and distinct vein populations between the Murray and Stimson formations (*Nachon et al., in prep*). Detailed analyses of crosscutting relationships between grey, light, and dark veins in the Pahrump Hills member indicate at least four separate vein-forming

events in this stratigraphic interval (*Kronyak et al., in revision*). Some sulfate vein formation could have occurred during deposition or early diagenetic stages during drier lake conditions (*Stein et al., 2018; Fedo et al., 2018*). Vein formation also likely extended into late diagenetic stages, as certain vein networks likely formed after burial at significant depths (*Caswell and Milliken, 2017*). Concretion formation in the Murray potentially occurred both before and after individual vein-forming events, producing the positive, crosscutting, and antithetical associations observed between these features **(Section 4.4)**. The distinct elemental enrichments in Mg, Ca, K, and Fe in some vein populations (*Kronyak et al., in revision*) are similar to enrichments observed in some concretions **(Figure 21)** and alteration halos (*Yen et al., 2018*) suggesting that vein, concretion, and alteration halo-forming events and fluids may be related.

After the Stimson formation was deposited, fluid events produced veins and Mg-enriched concretions in the lower Stimson formation (**Figure 22F,G**; *Hurowitz et al., 2017; Banham et al., 2018; Nachon et al., in prep*) that may have also affected the underlying Murray formation. We note that while it is also possible that the Murray fm. concretions **(Figure 22D)** could have formed after the emplacement of the Stimson fm., differences between the Murray and Stimson concretion populations suggest that they formed at different times. The Murray concretions exhibit a greater diversity of morphology **(Section 4.1)** and chemistry **(Section 6)** than the Stimson fm. concretions (e.g., **Figure 16**), which suggests that the Murray concretions likely formed before the Stimson concretions.

Alteration halos, crosscutting the Murray and Stimson formations and potentially coeval with some sulfate vein formation (*Yen et al., 2017*), later formed in a single or multiple fluid episodes (**Figure 22H***; Yen et al., 2017; Frydenvang et al., 2017*). These alteration halos likely postdate the Stimson concretion formation because similar concretion populations are observed both within and outside these alteration halos **(Figure 16; Section 4.4)**. Relatively recent post-depositional fluid processes at Gale crater have also been identified quantitatively from two-step K-Ar age dating of the Mojave_2 mudstone (*Martin et al., 2017*). Diagenetic jarosite was identified in this mudstone and dated to a formation age of 2 billion years old (*Martin et al., 2017;* **Figure 21J**), suggesting that aqueous processes could have occurred significantly after the initial deposition of the Murray sediments. This jarosite-forming event could also have been related to the dissolution of the gypsum laths and subsequent replacement by a pseudomorph material (**Figure 22I**; *Martin et al., 2017; Kah et al., 2018*).

To summarize our current understanding of depositional and diagenetic events at Gale crater from observations spanning Sols 750-1900, there are a minimum of six, if not more, aqueous episodes recorded in the diagenetic features observed in the Murray and Stimson formations: 1) Syn-depositional or early diagenetic crystal laths and sulfate vein formation, 2) Murray concretion formation that began or extended into late diagenetic stages after sediment compaction and lithification, 3) vein formation that crosscuts pre-existing concretions and veins, 4) concretion and vein formation in the Stimson formation, 5) alteration halo formation, and 6) formation of 2 Ga diagenetic jarosite in the Pahrump Hills mudstone.

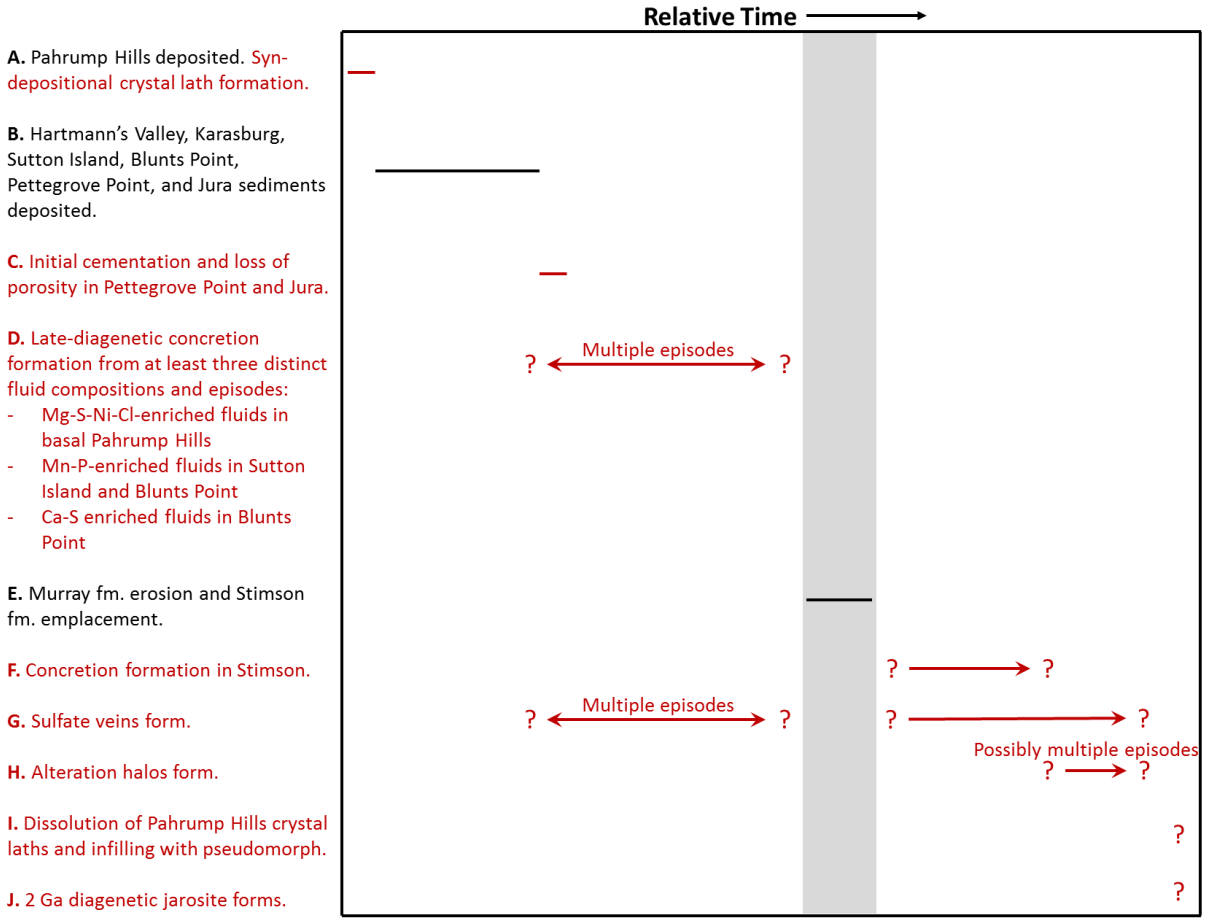

Figure 22. Relative timeline depicting when depositional and diagenetic features may have formed in the Murray formation. Letters are used to mark events discussed in **Section 8** and question marks indicate uncertainties of when events start or end. The grey region corresponds to the emplacement of the Stimson formation. The length of lines is not to scale. Black corresponds to primary depositional events, while red corresponds to syn-depositional or diagenetic formation of features. Please see **Section 8** for references to the literature.

9. Summary and Conclusions

The distribution of concretion properties – size, shape, chemistry, preservation of primary laminations, and relationships with other diagenetic features – throughout 300 meters of Murray formation reveal the following insights into diagenetic processes at Gale crater:

1. The Murray concretions likely formed in multiple fluid episodes, based on the diversity of their morphology, size, chemistry, and relationships with veins throughout the entire 300 m Murray section **(Section 7.3)**.
    a. Four major concretion assemblages are observed throughout the Murray formation **(Section 4.2)** and may reflect aqueous events at different times as host sediment properties changed after deposition, burial, and diagenesis. The basal section of Pahrump Hills uniquely hosts dendrites, and the rest of Pahrump Hills and Hartmann's Valley contain rough-textured irregular concretions and occasional spherules. The middle Murray members, Karasburg, Sutton Island, and Blunts Point, are characterized by prevalent spherules, flat concretions, and

smooth-textured irregular concretions. The uppermost Murray members explored as of Sol 1900, Pettegrove Point and Jura, host sparsely distributed and small smooth-textured irregular concretions.

b. Three major distinct chemical enrichments are associated with certain stratigraphic intervals and concretion assemblages, suggesting multiple fluid episodes with different compositions **(Section 6; Figure 21)**. The basal Pahrump Hills section is dominated by Mg-S-Ni-Cl enriched dendrites and irregular concretions. In Sutton Island and Blunt's Point, flat and some irregular concretions are enriched in Mn, P, and variable Fe, Mg, and Zn. A subset of concretions in Blunts Point may also exhibit Ca and S enrichments. Additional enrichments in K and Fe occur in more isolated intervals of the Murray.
c. Different size populations of spherules **(Figure 17)** and irregular concretions **(Figure 18)** suggest multiple precipitation events.
d. Complex relationships between concretions and veins suggest that concretions may predate and/or postdate veins, indicating multiple fluid episodes overall at Gale crater.

2. Many concretions in the Murray formed during late stages of diagenesis after sediment compaction and lithification, based on the following observations **(Section 7.2)**:
    a. Many concretions, in every Murray member, are observed to preserve primary host rock laminations without evidence for differential compaction around the concretion **(Figure 12,13)**.
    b. The upsection decrease in the maximum concretion size and the occurrence of mostly small millimeter-scale concretions in the Pettegrove Point and Jura members of the Vera Rubin Ridge **(Figure 18)** suggests that these smaller concretions formed after the initial cementation and loss of porosity in these ridge-forming rocks.
    c. Flat concretions may reflect formation along permeable bedding planes during later diagenesis. Lamination-enhancing features likely contain less mineral cement than discrete concretions, as the result of forming after sediment compaction when there is less porosity available to fill.
3. The observations of late diagenetic concretions in all of the Murray members **(Figure 13)**, as well as the identification of distinct elemental enrichments corresponding to concretion assemblages at certain stratigraphic intervals **(Figure 21)**, allows for timing constraints to be placed on late stage fluid chemistry at Gale crater.
4. There were at least six post-depositional events that occurred at Gale crater and formed the full suite of diagenetic features observed in the Murray and Stimson formations. (**Section 8**; see references therein). 1) Syn-depositional crystal laths and sulfate veins formed, followed by 2) late diagenetic concretion-forming episodes with varying fluid chemistries in the Murray formation. 3) Crosscutting veins formed in the Murray prior to Stimson emplacement. 4) Concretions and veins then formed in the Stimson formation, followed by 5) alteration halos and 6) the formation of diagenetic jarosite two billion years ago.

Acknowledgements: We are indebted to the MSL team of engineers and scientists for maintaining this mission and collecting the data used in this work. We are very grateful for the positive and constructive reviews provided by two anonymous reviewers. We also thank Fred

Calef for providing lists of instrument observations that facilitated this work and Nicholas Ruoff, Amy Culver, and Bob Deen for help in generating orthorectified Mastcam images. This research was carried out at the Jet Propulsion Laboratory, California Institute of Technology, under a contract with the National Aeronautics and Space Administration. Co-authors in the United States were funded by the NASA Mars Exploration program.

Declarations of interest: none.

References

Allison, P. A., & Pye, K. (1994). Early Diagenetic Mineralization and Fossil Preservation in Modern Carbonate Concretions. *PALAIOS*, *9*(6), 561–575. https://doi.org/10.2307/3515128

Banham, S. G., Gupta, S., Rubin, D. M., Watkins, J. A., Sumner, D. Y., Edgett, K. S., et al. (2018). Ancient Martian aeolian processes and palaeomorphology reconstructed from the Stimson formation on the lower slope of Aeolis Mons, Gale crater, Mars. *Sedimentology*, *65*(4), 993–1042. https://doi.org/10.1111/sed.12469

Bell, J. F., Godber, A., McNair, S., Caplinger, M. A., Maki, J. N., Lemmon, M. T., et al. (2017). The Mars Science Laboratory Curiosity rover Mastcam instruments: Preflight and in-flight calibration, validation, and data archiving. *Earth and Space Science*, *4*(7), 396–452. https://doi.org/10.1002/2016EA000219

Berner, R. A. (1968). Rate of concretion growth. *Geochimica et Cosmochimica Acta*, *32*(5), 477–483. https://doi.org/10.1016/0016-7037(68)90040-9

Bowen, B. B., Benison, K. C., Oboh-Ikuenobe, F. E., Story, S., & Mormile, M. R. (2008). Active hematite concretion formation in modern acid saline lake sediments, Lake Brown, Western Australia. *Earth and Planetary Science Letters*, *268*(1), 52–63. https://doi.org/10.1016/j.epsl.2007.12.023

Calvin, W. M., Shoffner, J. D., Johnson, J. R., Knoll, A. H., Pocock, J. M., Squyres, S. W., et al. (2008). Hematite spherules at Meridiani: Results from MI, Mini-TES, and Pancam. *Journal of Geophysical Research: Planets*, *113*(E12). https://doi.org/10.1029/2007JE003048

Caswell, T. E., & Milliken, R. E. (2017). Evidence for hydraulic fracturing at Gale crater, Mars: Implications for burial depth of the Yellowknife Bay formation. *Earth and Planetary Science Letters*, *468*, 72–84. https://doi.org/10.1016/j.epsl.2017.03.033

Chan, M. A., Parry, W. T., & Bowman, J. R. (2000). Diagenetic Hematite and Manganese Oxides and Fault-Related Fluid Flow in Jurassic Sandstones, Southeastern Utah. *AAPG Bulletin*, *84*(9), 1281–1310. https://doi.org/10.1306/A9673E82-1738-11D7-8645000102C1865D

Chan, M. A., Bowen, B. B., Parry, W. T., Ormö, J., & Komatsu, G. (2005). Red rock and red planet diagenesis: Comparisons of Earth and Mars concretions. *GSA Today*, *15*(8), 4–10. https://doi.org/10.1130/1052-5173(2005)015

Chan, M. A., Ormö, J., Park, A. J., Stich, M., Souza-Egipsy, V., & Komatsu, G. (2007). Models of iron oxide concretion formation: field, numerical, and laboratory comparisons. *Geofluids*, *7*(3), 356–368. https://doi.org/10.1111/j.1468-8123.2007.00187.x

Chan, Marjorie A., Beitler, B., Parry, W. T., Ormö, J., & Komatsu, G. (2004). A possible terrestrial analogue for haematite concretions on Mars. *Nature*, *429*(6993), 731–734. https://doi.org/10.1038/nature02600

Clark, P. J., & Evans, F. C. (1954). Distance to Nearest Neighbor as a Measure of Spatial Relationships in Populations. Ecology, 35(4), 445–453. https://doi.org/10.2307/1931034

Clegg, S. M., Wiens, R. C., Anderson, R., Forni, O., Frydenvang, J., Lasue, J., et al. (2017). Recalibration of the Mars Science Laboratory ChemCam instrument with an expanded geochemical database. *Spectrochimica Acta Part B: Atomic Spectroscopy*, *129*, 64–85. https://doi.org/10.1016/j.sab.2016.12.003

Coleman, M. L. (1993). Microbial processes: Controls on the shape and composition of carbonate concretions. *Marine Geology*, *113*(1), 127–140. https://doi.org/10.1016/0025-3227(93)90154-N

Day-Stirrat, R. J., Flemings, P. B., You, Y., Aplin, A. C., & van der Pluijm, B. A. (2012). The fabric of consolidation in Gulf of Mexico mudstones. *Marine Geology*, *295–298*, 77–85. https://doi.org/10.1016/j.margeo.2011.12.003

Edgar, L. A., A. A. Fraeman, S. Gupta, C. M. Fedo, J. P. Grotzinger, K. M. Stack, K. A. Bennett, V. Z. Sun, S. G. Banham, N. T. Stein, K. S. Edgett, D. M. Rubin, J. Van Beek. (2018) Sedimentology and stratigraphy observed at Vera Rubin Ridge by the Mars Science Laboratory Curiosity rover. 49th Lunar and Planetary Science Conference, Abstract #1704.

Edgett, K. S., Yingst, R. A., Ravine, M. A., Caplinger, M. A., Maki, J. N., Ghaemi, F. T., et al. (2012). Curiosity's Mars Hand Lens Imager (MAHLI) Investigation. *Space Science Reviews*, *170*(1–4), 259–317. https://doi.org/10.1007/s11214-012-9910-4

Fedo, C. M., J. P. Grotzinger, S. Gupta, A. Fraeman, L. Edgar, K. Edgett, N. Stein, F. Rivera-Hernandez, K. Lewis, K. M. Stack, C. House, D. Rubin, A. R. Vasavada. (2018) Sedimentology and stratigraphy of the Murray formation, Gale crater, Mars. 49th Lunar and Planetary Science Conference, Abstract #2078.

Fischer, W.W. and Knoll, A.H. (2009) An iron shuttle for deep-water silica in Late Archean and Early Paleoproterozoic iron formation, *Geological Society of America Bulletin*, *121*, 222-235.

Fraeman, A. A., Ehlmann, B. L., Arvidson, R. E., Edwards, C. S., Grotzinger, J. P., Milliken, R. E., et al. (2016). The stratigraphy and evolution of lower Mount Sharp from spectral, morphological, and thermophysical orbital data sets. *Journal of Geophysical Research: Planets*, *121*(9), 1713–1736. https://doi.org/10.1002/2016JE005095

Frydenvang, J., Gasda, P. J., Hurowitz, J. A., Grotzinger, J. P., Wiens, R. C., Newsom, H. E., et al. (2017). Diagenetic silica enrichment and late-stage groundwater activity in Gale crater, Mars. *Geophysical Research Letters*, *44*(10), 4716–4724. https://doi.org/10.1002/2017GL073323

Gasda,P. J., N. L. Lanza, S. N. Lamm, J. L'Haridon, P.-Y. Meslin, O. Forni, J. Frydenvang, N. Stein, W. Fischer, F. Rivera-Hernandez, H. E. Newsom, B. Clark, R. C. Wiens, S. M. Clegg, S. Maurice. (2018). Evidence of redox sensitive elements associated with possible shoreline deposits in Gale crater. 49th Lunar and Planetary Science Conference, Abstract #2483.

Gasparatos, D. (2012). Fe–Mn Concretions and Nodules to Sequester Heavy Metals in Soils. In *Environmental Chemistry for a Sustainable World* (pp. 443–474). Springer, Dordrecht. https://doi.org/10.1007/978-94-007-2439-6_11

Gellert, R., B. C. Clark and the MSL and MER Science Teams (2015), In situ compositional measurements of rocks and soils with the Alpha Particle X-ray Spectrometer on NASA's Mars Rover, Elements 11, 39-44, doi: 10.2113/gselements.11.1.39

Grotzinger, J. P., Sumner, D. Y., Kah, L. C., Stack, K., Gupta, S., Edgar, L., et al. (2014). A Habitable Fluvio-Lacustrine Environment at Yellowknife Bay, Gale Crater, Mars. *Science*, *343*(6169), 1242777. https://doi.org/10.1126/science.1242777

Grotzinger, J. P., Gupta, S., Malin, M. C., Rubin, D. M., Schieber, J., Siebach, K., et al. (2015). Deposition, exhumation, and paleoclimate of an ancient lake deposit, Gale crater, Mars. *Science*, *350*(6257), aac7575. https://doi.org/10.1126/science.aac7575

Gwizd, S., C. Fedo, J. Grotzinger, K. Edgett, F. Rivera-Hernandez, N. Stein. (2018). Depositional history of the Hartmann's Valley member, Murray formation, Gale crater, Mars. 49th Lunar and Planetary Science Conference, Abstract #2150.

Huggett, J. M. (1993). Diagenesis of Mudrocks and Concretions from the London Clay Formation in the London Basin. *Clay Minerals*, *29*, 693–707. https://doi.org/10.1180/claymin.1994.029.4.22

Hurowitz, J.A., Grotzinger, J.P., Fischer, W.W., McLennan, S.M., Milliken, R.E., Stein, N., Vasavada, A.R., Blake, D.F., Dehouck, E., Eigenbrode, J.L., Fairén, A.G., Frydenvang, J., Gellert, R., Grant, J.A., Gupta, S., Herkenhoff, K.E., Ming, D.W., Rampe, E.B., Schmidt, M.E., Siebach, K.L., Stack-Morgan, K., Sumner, D.Y., Wiens, R.C., 2017. Redox stratification of an ancient lake in Gale crater, Mars. Science (80-.). 356.

Kah, L. C., R. Kronyak, J. Van Beek, M. Nachon, N. Mangold, L. Thompson, R. Wiens, J. Grotzinger, J. Farmer, M. Minitti, J. Schieber, D. Oehler. (2015) Diagenetic crystal clusters and dendrites, Lower Mount Sharp, Gale crater. 46th Lunar and Planetary Science Conference, Abstract #1901.

Kah, L. C., Stack, K. M., Eigenbrode, J. L., Yingst, R. A., & Edgett, K. S. (2018). Syndepositional precipitation of calcium sulfate in Gale crater, Mars. Terra Nova. In press. https://doi.org/10.1111/ter.12359

Kronyak, R. E., Kah, L. C., Nachon, M., Mangold, N., Wiens, R. C., Williams, R., Schieber, J., Grotzinger, J. (2015) Distribution of mineralized veins from Yellowknife Bay to Mount Sharp, Gale Crater, Mars: Insight from Textural and Compositional Variation. 46th Lunar and Planetary Science Conference, Abstract #1903.

Kronyak, R. E., Kah, L. C. et al. Mineral-filled fractures as indicators of multigenerational fluid events in the basal Murray formation, Gale crater, Mars. In preparation.

Lamm, S. N., N. L. Lanza, P. J. Gasda, R. C. Wiens, P.-Y. Meslin, M. F. Kirk. (2018) Manganese observations from ChemCam during Sols 1650-1750: Implications for a changing redox environment. 49th Lunar and Planetary Science Conference, Abstract #1447.

Lash, G. G., & Blood, D. (2004). Geochemical and textural evidence for early (shallow) diagenetic growth of stratigraphically confined carbonate concretions, Upper Devonian Rhinestreet black shale, western New York. *Chemical Geology*, *206*(3), 407–424. https://doi.org/10.1016/j.chemgeo.2003.12.017

L'Haridon, J., Mangold, N., Meslin, P.-Y., Johnson, J. R., Rapin, W., Forni, O., et al. (2018). Chemical variability in mineralized veins observed by ChemCam on the lower slopes of Mount Sharp in Gale crater, Mars. *Icarus*, *311*, 69–86. https://doi.org/10.1016/j.icarus.2018.01.028

Marshall, J. D., & Pirrie, D. (2013). Carbonate concretions—explained. *Geology Today*, *29*(2), 53–62. https://doi.org/10.1111/gto.12002

Martin, P. E., Farley, K. A., Baker, M. B., Malespin, C. A., Schwenzer, S. P., Cohen, B. A., et al. (2017). A Two-Step K-Ar Experiment on Mars: Dating the Diagenetic Formation of Jarosite from Amazonian Groundwaters. *Journal of Geophysical Research: Planets*, *122*(12), 2803–2818. https://doi.org/10.1002/2017JE005445

Maurice S., et al. (2012) The ChemCam Instruments on the Mars Science Laboratory (MSL) Rover: Science Objectives and Mast Unit. Spa. Sci. Rev. 170, 95-166. https://doi.org/10.1007/s11214-012-9912-2

McBride, Abdel-Wahab, A., & El-Younsy, A. R. M. (1999). Origin of spheroidal chert nodules, Drunka Formation (Lower Eocene), Egypt. *Sedimentology*, *46*(4), 733–755. https://doi.org/10.1046/j.1365-3091.1999.00253.x

McBride, E. F., & Parea, G. C. (2001). Origin of Highly Elongate, Calcite-Cemented Concretions in Some Italian Coastal Beach and Dune Sands. *Journal of Sedimentary Research*, *71*(1), 82–87. https://doi.org/10.1306/041900710082

McLennan, S. M., Bell, J. F., Calvin, W. M., Christensen, P. R., Clark, B. C., de Souza, P. A., et al. (2005). Provenance and diagenesis of the evaporite-bearing Burns formation, Meridiani Planum, Mars. *Earth and Planetary Science Letters*, *240*(1), 95–121. https://doi.org/10.1016/j.epsl.2005.09.041

Meslin, P.-Y., P. Gasda, J. L'Haridon, O. Forni, N. Lanza, S. Lamm, J. R. Johnson, R. C. Wiens, L. Thompson, W. Rapin, O. Gasnault, A. Cousin, N. Mangold, E. Dehouck, S. Maurice, J. Frydenvang, J. Lasue. (2018). Detection of hydrous manganese and iron oxides with variable phosphorous and magnesium contents in the lacustrine sediments of the Murray formation, Gale, Mars. 49th Lunar and Planetary Science Conference, Abstract #1447.

Minitti, M.E., J. Van Beek, F. J. Calef III, D. Harker, K. E. Herkenhoff, L. C. Kah, M. R. Kennedy, G. M. Krezoski, L. Lipkaman, B. Nixon, S. K. Rowland, J. Schieber, K. M. Stack, R. A. Yingst. (2018) Primary and secondary features within the Pahrump Hills outcrop as seen in the MARDI sidewalk mosaic. 49th Lunar and Planetary Science Conference, Abstract #1560.

Mozley, P. S. (1996). The internal structure of carbonate concretions in mudrocks: a critical evaluation of the conventional concentric model of concretion growth. *Sedimentary Geology*, *103*(1), 85–91. https://doi.org/10.1016/0037-0738(95)00087-9

Mozley,P.S. (2003) Diagenetic structures. In: Encyclopedia of Sediments and Sedimentary Rocks (ed. Middleton G), pp. 219–25. Kluwer Academic Press, Dordrecht.

Nachon, M., Clegg, S. M., Mangold, N., Schröder, S., Kah, L. C., Dromart, G., et al. (2014). Calcium sulfate veins characterized by ChemCam/Curiosity at Gale crater, Mars. *Journal of Geophysical Research: Planets*, *119*(9), 1991–2016. https://doi.org/10.1002/2013JE004588

Nachon, M., Mangold, N., Forni, O., Kah, L. C., Cousin, A., Wiens, R. C., et al. (2016). Chemistry of diagenetic features analyzed by ChemCam at Pahrump Hills, Gale crater, Mars. *Icarus*, *281*, 121–136. https://doi.org/10.1016/j.icarus.2016.08.026

Nachon, M. et al. Stratigraphic distribution of veins within the Murray and Stimson formations: Implications for groundwater circulation at Gale crater, Mars. In preparation.

Oertel, G., & Curtis, C. D. (1972). Clay-Ironstone Concretion Preserving Fabrics Due to Progressive Compaction. *GSA Bulletin*, *83*(9), 2597–2606. https://doi.org/10.1130/0016-7606(1972)83[2597:CCPFDT]2.0.CO;2

Pearson, M. J. (1979). Geochemistry of the Hepworth Carboniferous sediment sequence and origin of the diagenetic iron minerals and concretions. *Geochimica et Cosmochimica Acta*, *43*(6), 927–941. https://doi.org/10.1016/0016-7037(79)90230-8

Potter, S. L., & Chan, M. A. (2011). Joint controlled fluid flow patterns and iron mass transfer in Jurassic Navajo Sandstone, Southern Utah, USA. *Geofluids, 11(2)*, 184–198. https://doi.org/10.1111/j.1468-8123.2011.00329.x

Potter, S. L., Chan, M. A., Petersen, E. U., Dyar, M. D., & Sklute, E. (2011). Characterization of Navajo Sandstone concretions: Mars comparison and criteria for distinguishing diagenetic origins. *Earth and Planetary Science Letters, 301(3–4),* 444–456. https://doi.org/10.1016/j.epsl.2010.11.027

Potter-McIntyre, S.L., Chan, M.A., McPherson, B.J. (2014). Concretion formation in volcaniclastic host rocks: evaluating the role of organics, mineralogy, and geochemistry on early diagenesis. J. Sediment. Res. 84, 875–892.

Pye, K. (1981). Marshrock formed by iron sulphide and siderite cementation in saltmarsh sediments. *Nature*, *294*(5842), 650–652. https://doi.org/10.1038/294650a0

Raiswell, R. (1988). Evidence for surface reaction-controlled growth of carbonate concretions in shales. *Sedimentology*, *35*(4), 571–575. https://doi.org/10.1111/j.1365-3091.1988.tb01236.x

Raiswell, R., & Fisher, Q. J. (2000). Mudrock-hosted carbonate concretions: a review of growth mechanisms and their influence on chemical and isotopic composition. *Journal of the Geological Society*, *157*(1), 239–251. https://doi.org/10.1144/jgs.157.1.239

Rampe, E. B., Ming, D. W., Blake, D. F., Bristow, T. F., Chipera, S. J., Grotzinger, J. P., et al. (2017). Mineralogy of an ancient lacustrine mudstone succession from the Murray formation, Gale crater, Mars. *Earth and Planetary Science Letters*, *471*, 172–185. https://doi.org/10.1016/j.epsl.2017.04.021

Rapin, W., B. Ehlmann, J. Grotzinger, G. Dromart, S. Clegg, L. Thompson, V. Fox, R.C. Wiens, O. Forni, T.S.J. Gabriel, C. Hardgrove, Briny waters evidenced by magnesium sulfate rich layers discovered in situ at Gale crater. (2018) 49th Lunar and Planetary Science Conference, Abstract #2936.

Rice, M. S., Gupta, S., Treiman, A. H., Stack, K. M., Calef, F., Edgar, L. A., et al. (2017). Geologic overview of the Mars Science Laboratory rover mission at the Kimberley, Gale crater, Mars. *Journal of Geophysical Research: Planets*, *122*(1), 2–20. https://doi.org/10.1002/2016JE005200

Schieber, J., D. Sumner, D. Bish, K. Stack, M. Minitti, A. Yingst, K. Edgett, M. Malin, J. Grotzinger, The MSL Science Team. (2015) The Pahrump succession in Gale crater – A potential evaporate bearing lacustrine mudstone with resemblance to Earth analogs. 46th Lunar and Planetary Science Conference, Abstract #2153.

Sefton-Nash, E., & Catling, D. C. (2008). Hematitic concretions at Meridiani Planum, Mars: Their growth timescale and possible relationship with iron sulfates. *Earth and Planetary Science Letters*, *269*(3), 366–376. https://doi.org/10.1016/j.epsl.2008.02.009

Seilacher, A. (2001). Concretion morphologies reflecting diagenetic and epigenetic pathways. *Sedimentary Geology*, *143*(1), 41–57. https://doi.org/10.1016/S0037-0738(01)00092-6

Sellés-Martínez, J. (1996). Concretion morphology, classification and genesis. *Earth-Science Reviews*, *41*(3), 177–210. https://doi.org/10.1016/S0012-8252(96)00022-0

Siebach, K. L., Grotzinger, J. P., Kah, L. C., Stack, K. M., Malin, M., Léveillé, R., & Sumner, D. Y. (2014). Subaqueous shrinkage cracks in the Sheepbed mudstone: Implications for early fluid diagenesis, Gale crater, Mars. *Journal of Geophysical Research: Planets*, *119*(7), 1597–1613. https://doi.org/10.1002/2014JE004623

Stack, K. M., Grotzinger, J. P., Kah, L. C., Schmidt, M. E., Mangold, N., Edgett, K. S., et al. (2014). Diagenetic origin of nodules in the Sheepbed member, Yellowknife Bay formation, Gale crater, Mars. *Journal of Geophysical Research: Planets*, *119*(7), 1637–1664. https://doi.org/10.1002/2014JE004617

Stack, K. M., Grotzinger, J. P., Lamb, M. P., Gupta, S., Rubin, D. M., Kah, L. C., et al. (2018). Evidence for plunging river plume deposits in the Pahrump Hills member of the Murray formation, Gale crater, Mars. Sedimentology. https://doi.org/10.1111/sed.12558

Stein, N., Grotzinger, J. P., Schieber, J., Mangold, N., Hallet, B., Newsom, H., et al. (2018). Desiccation cracks provide evidence of lake drying on Mars, Sutton Island member, Murray formation, Gale Crater. *Geology*, *46*(6), 515–518. https://doi.org/10.1130/G40005.1

Thompson, L. M., R. Gellert, J. G. Spray, L. C. Kah and the APXS and MSL Science Teams (2015) The composition of the basal Murray formation at Pahrump Hills, Gale crater. Mars. Presented at *46th Lunar and Planetary Science Conference, Woodlands, Texas, March 16th - 20th, 2015*, 1429.pdf

Thompson, L. M., R. Gellert, J. G. Spray, L. C. Kah and the APXS and MSL Science Teams (2017) Recent compositional trends within the Murray formation, Gale crater, Mars, as seen by APXS: Implications for sedimentary, diagenetic and alteration history. Presented at *2017 **AGU** Fall Meeting*, New Orleans, LA, 11-15 Dec 2017, P31A-2790.

VanBommel, S. J., R. Gellert, J. A. Berger, J. L. Campbbell, L. M. Thompson, K. S. Edgett, et al. (2016) Deconvolution of distinct lithology chemistry through oversampling with the Mars Science Laboratory Alpha Particle X-ray Spectrometer. X-ray Spectrometry, 45, 155-161. **https://doi.org/10.1002/xrs.2681**

VanBommel, S. J., Gellert, R., Berger, J. A., Thompson, L. M., Edgett, K. S., McBride, M. J., et al. (2017). Modeling and mitigation of sample relief effects applied to chemistry measurements by the Mars Science Laboratory Alpha Particle X-ray Spectrometer. *X-Ray Spectrometry*, *46*(4), 229–236. https://doi.org/10.1002/xrs.2755

Wiens, R. C., Maurice, S., Barraclough, B., Saccoccio, M., Barkley, W. C., Bell, J. F., et al. (2012). The ChemCam instrument suite on the Mars Science Laboratory (MSL) rover: Body unit and combined system tests. *Space Science Reviews*, *170*(1–4), 167–227. https://doi.org/10.1007/s11214-012-9902-4

Wiens, R. C., Rubin, D. M., Goetz, W., Fairén, A. G., Schwenzer, S. P., Johnson, J. R., et al. (2017). Centimeter to decimeter hollow concretions and voids in Gale Crater sediments, Mars. *Icarus*, *289*, 144–156. https://doi.org/10.1016/j.icarus.2017.02.003

Yen, A. S., Ming, D. W., Vaniman, D. T., Gellert, R., Blake, D. F., Morris, R. V., et al. (2017). Multiple stages of aqueous alteration along fractures in mudstone and sandstone strata in Gale Crater, Mars. *Earth and Planetary Science Letters*, *471*, 186–198. https://doi.org/10.1016/j.epsl.2017.04.033

Yen, A. S., R. Gellert, L. M. Thompson, A. H. Treiman, R. V. Morris, D. T. Vaniman, B. C. Clark, J. A. Berger, R. E. Kronyak. (2018) Mobility of potassium-rich fluids on Mars: Implications for diagenesis. 49th Lunar and Planetary Science Conference, Abstract #2690.